

The kaobook class

**Use this document as a template**

# **Millikelvin Confocal Microscopy of Semiconductor Membranes and Filter Functions for Unital Quantum Operations**

**Customise this page according to your needs**

Tobias Hangleiter\*

August 5, 2025

\* A  $\text{\LaTeX}$  lover/hater

The harmony of the world is made manifest in Form and Number, and the heart and soul and all the poetry of Natural Philosophy are embodied in the concept of mathematical beauty.

– D'Arcy Wentworth Thompson

# Contents

<b>Contents</b>	<b>iii</b>
<b>I A FLEXIBLE PYTHON TOOL FOR FOURIER-TRANSFORM NOISE SPECTROSCOPY</b>	<b>1</b>
<b>1 Introduction</b>	<b>2</b>
<b>2 Theory of spectral noise estimation</b>	<b>4</b>
2.1 Spectrum estimation from time series . . . . .	5
2.2 Window functions . . . . .	7
2.3 Welch's method . . . . .	8
2.4 Parameters & Properties of the PSD . . . . .	9
<b>3 The python_spectrometer software package</b>	<b>11</b>
3.1 Package design and implementation . . . . .	11
3.1.1 Data acquisition . . . . .	11
3.1.2 Data processing . . . . .	13
3.2 Feature overview . . . . .	14
3.2.1 Serial spectrum acquisition . . . . .	15
3.2.2 Live spectrum acquisition . . . . .	18
<b>4 Conclusion and outlook</b>	<b>20</b>
<b>II CHARACTERIZATION AND IMPROVEMENTS OF A MILLIKELVIN CONFOCAL MICROSCOPE</b>	<b>23</b>
<b>1 Introduction</b>	<b>3</b>
<b>2 Characterization of the cryostat performance</b>	<b>4</b>
2.1 Cooling power . . . . .	4
2.2 Electron temperature . . . . .	6
<b>3 Optical path</b>	<b>10</b>
3.1 Light coupling . . . . .	10
3.1.1 Choosing lenses . . . . .	10
3.1.2 Collection efficiency . . . . .	13
3.1.3 Imaging the laser spot . . . . .	16
3.1.4 Cross-polarization extinction . . . . .	17
3.2 Exemplary measurement of non-classical light . . . . .	17
<b>4 Vibration noise</b>	<b>19</b>
4.1 Vibration isolation . . . . .	20
4.1.1 Damping theory . . . . .	20
4.1.2 Microscope isolation concept . . . . .	21
4.2 Accelerometric vibration spectroscopy . . . . .	21
4.3 Optical vibration spectroscopy . . . . .	23
4.3.1 Noise floor . . . . .	26
4.4 Routes for improvement . . . . .	28
<b>5 Conclusion &amp; outlook</b>	<b>30</b>

<b>III OPTICAL MEASUREMENTS OF ELECTROSTATIC EXCITON TRAPS IN SEMICONDUCTOR MEMBRANES</b>	<b>31</b>
<b>6 Introduction</b>	<b>32</b>
<b>7 Photoluminescence and excitons in semiconductors</b>	<b>33</b>
7.1 Photoluminescence in doped GaAs/Al <sub>x</sub> Ga <sub>1-x</sub> As heterostructures . . . . .	33
7.2 The quantum-confined Stark effect . . . . .	34
7.2.1 In-plane confinement . . . . .	36
7.3 Excitonic complexes . . . . .	39
<b>8 The mjolnir measurement framework</b>	<b>40</b>
<b>9 Observations</b>	<b>41</b>
9.1 Photoluminescence spectroscopy . . . . .	42
9.1.1 Quantum-confined Stark shift . . . . .	43
9.1.2 Power dependence . . . . .	45
9.1.3 Spatial dependence . . . . .	47
9.2 Photoluminescence excitation spectroscopy . . . . .	49
9.3 Transfer-matrix method simulations of the membrane structure . . . . .	51
<b>10 Conclusion &amp; outlook</b>	<b>55</b>
<b>IV A FILTER-FUNCTION FORMALISM FOR UNITAL QUANTUM OPERATIONS</b>	<b>56</b>
<b>APPENDIX</b>	<b>57</b>
<b>A Optical coupling</b>	<b>34</b>
A.1 Collection efficiency . . . . .	34
A.2 Mode profile . . . . .	35
A.3 Fraunhofer diffraction . . . . .	36
<b>B Vibration spectroscopy</b>	<b>38</b>
B.1 Knife-edge measurement . . . . .	38
B.2 Additional vibration spectroscopy data . . . . .	38
<b>C Additional TMM simulations</b>	<b>39</b>
C.1 Dependence on epoxy thickness . . . . .	39
C.2 Optimization of the barrier thickness . . . . .	39
<b>D Additional measurements</b>	<b>40</b>
<b>Bibliography</b>	<b>41</b>
<b>List of Terms</b>	<b>45</b>
<b>Declaration of Authorship</b>	<b>46</b>

# List of Figures

2.1	Generated by <code>img/tikz/spectrometer/lockin_dut.tex</code> . . . . .	4
2.2	Generated by <code>img/py/spectrometer/lorentz.py</code> . . . . .	6
2.3	Generated by <code>img/py/spectrometer/pyspeck.py</code> . . . . .	8
2.4	Generated by <code>img/py/spectrometer/pyspeck.py</code> . . . . .	8
2.5	Generated by <code>img/py/spectrometer/pyspeck.py</code> . . . . .	9
2.6	Generated by <code>img/tikz/spectrometer/daq_settings.tex</code> . . . . .	10
3.1	Generated by <code>img/tikz/spectrometer/speck_tree.tex</code> . . . . .	11
3.2	Generated by <code>img/py/spectrometer/pyspeck_workflow.py</code> . . . . .	15
3.3	Generated by <code>img/py/spectrometer/pyspeck_workflow.py</code> . . . . .	16
3.4	Generated by <code>img/py/spectrometer/pyspeck_workflow.py</code> . . . . .	17
3.5	Generated by <code>img/py/spectrometer/pyspeck_workflow.py</code> . . . . .	17
3.6	Generated by <code>img/py/spectrometer/pyspeck_workflow.py</code> . . . . .	17
3.7	Generated by <code>img/py/spectrometer/pyspeck_workflow.py</code> . . . . .	18
3.8	Generated by <code>img/py/spectrometer/pyspeck_live_view.py</code> . . . . .	19
2.1	Generated by <code>img/py/setup/cooling_power.py</code> . . . . .	5
2.2	Generated by <code>img/py/setup/cooling_power.py</code> . . . . .	6
2.3	Generated by <code>img/py/setup/cooling_power.py</code> . . . . .	6
2.4	Generated by <code>img/py/setup/transport.py</code> . . . . .	7
2.5	Generated by <code>img/py/setup/transport.py</code> . . . . .	8
2.6	Generated by <code>img/py/setup/transport.py</code> . . . . .	9
3.1	Generated by <code>img/tikz/setup/optical_path.tex</code> . . . . .	10
3.2	Generated by <code>img/py/setup/single_mode_fiber_coupling.py</code> . . . . .	13
3.3	Generated by <code>img/tikz/setup/emission.tex</code> . . . . .	14
3.4	Generated by <code>img/py/setup/extraction.py</code> . . . . .	15
3.5	Generated by <code>img/py/setup/extraction.py</code> . . . . .	16
3.6	Generated by <code>img/py/setup/imaging.py</code> . . . . .	17
3.7	Generated by <code>img/py/setup/g2.py</code> . . . . .	18
3.8	Generated by <code>img/py/setup/g2.py</code> . . . . .	18
4.1	Generated by <code>img/pdf/setup/springs.py</code> . . . . .	20
4.2	Generated by <code>img/py/setup/vibration_spectroscopy.py</code> . . . . .	23
4.3	Generated by <code>img/tikz/setup/knife_edge.tex</code> . . . . .	23
4.4	Generated by <code>img/py/setup/vibration_spectroscopy.py</code> . . . . .	24
4.5	Generated by <code>img/py/setup/vibration_spectroscopy.py</code> . . . . .	24
4.6	Generated by <code>img/py/setup/vibration_spectroscopy.py</code> . . . . .	25
4.7	Generated by <code>img/py/setup/vibration_spectroscopy.py</code> . . . . .	26
4.8	Generated by <code>img/pdf/setup/vibration_spectroscopy.py</code> . . . . .	28
5.1	Generated by <code>img/py/setup/vibration_spectroscopy.py</code> . . . . .	30
7.1	Generated by <code>img/py/experiment/pl.py</code> . . . . .	33
7.2	Generated by <code>img/py/experiment/qcse.py</code> . . . . .	34
7.3	Generated by <code>img/py/experiment/qcse.py</code> . . . . .	35
7.4	Generated by <code>img/py/experiment/qcse.py</code> . . . . .	37
7.5	Generated by <code>img/py/experiment/qcse.py</code> . . . . .	38
8.1	Generated by <code>img/tikz/experiment/mjolnir_tree.tex</code> . . . . .	40

9.1	Sample: Doped M1_05_49-2. $\lambda_{\text{exc}} = 795 \text{ nm}$ . $P = 0.92 \mu\text{W}$ . Generated by img/py/experiment/pl.py. . . . .	42
9.2	Sample: Honey H13. $\lambda_{\text{exc}} = 795 \text{ nm}$ . $P = 1 \mu\text{W}$ . Generated by img/py/experiment/pl.py. . . . .	43
9.3	Sample: Doped M1_05_49-2. $V_{\text{CM}} = -1.3 \text{ V}$ . $\lambda_{\text{exc}} = 795 \text{ nm}$ . $P = 10 \mu\text{W}$ . Generated by img/py/experiment/pl.py. . . . .	44
9.4	Sample: Doped M1_05_49-2. $V_{\text{DM}} = -2.7 \text{ V}$ . $V_{\text{CM}} = -1.3 \text{ V}$ . $\lambda_{\text{exc}} = 795 \text{ nm}$ . Generated by img/py/experiment/pl.py. . . . .	45
9.5	Sample: Doped M1_05_49-2. $V_{\text{B}} = 0 \text{ V}$ . Generated by img/py/experiment/pl.py. . . . .	47
9.6	Sample: Fig F10. $\lambda_{\text{exc}} = 795 \text{ nm}$ . $V_y = 30 \text{ V}$ Generated by img/py/experiment/pl.py. . . . .	47
9.7	Sample: Doped M1_05_49-2. $V_{\text{DM}} = -0.43 \text{ V}$ . $V_{\text{CM}} = -3.75 \text{ V}$ . $V_y = V_z = 30 \text{ V}$ $P = 1 \mu\text{W}$ . $\lambda_{\text{exc}} = 795 \text{ nm}$ . Generated by img/py/experiment/pl.py. . . . .	48
9.8	Sample: Doped M1_05_49-2. $V_{\text{CM}} = -1.3 \text{ V}$ . $P = 1 \mu\text{W}$ . Generated by img/py/experiment/ple.py. . . . .	50
9.9	Generated by img/py/experiment/tmm.py. . . . .	53
9.10	Generated by img/py/experiment/tmm.py. . . . .	53
9.11	Generated by img/py/experiment/tmm.py. . . . .	54
9.12	Generated by img/py/experiment/tmm.py. . . . .	54
B.1	. . . . .	38
C.1	Generated by img/py/experiment/tmm.py. . . . .	39
C.2	Generated by img/py/experiment/tmm.py. . . . .	39
D.1	Sample: Doped M1_05_49-2. $\lambda_{\text{exc}} = 795 \text{ nm}$ . Generated by img/py/experiment/pl.py. . . . .	40
D.2	Sample: Doped M1_05_49-2. $V_{\text{CM}} = -1.3 \text{ V}$ . $P = 1 \mu\text{W}$ . Generated by img/py/experiment/ple.py. . . . .	40

**Part I**

**A FLEXIBLE PYTHON TOOL FOR  
FOURIER-TRANSFORM NOISE  
SPECTROSCOPY**

## **Part II**

# **CHARACTERIZATION AND IMPROVEMENTS OF A MILLIKELVIN CONFOCAL MICROSCOPE**



**Part III**

**OPTICAL MEASUREMENTS OF  
ELECTROSTATIC EXCITON TRAPS IN  
SEMICONDUCTOR MEMBRANES**

# Introduction

6



# Photoluminescence and excitons in semiconductors

7

**T**HE development of remote-doping techniques enabled the growth of extremely high-mobility two-dimensional electron gases (2DEGs) in GaAs/Al<sub>x</sub>Ga<sub>1-x</sub>As heterostructures [1]. In these structures, dopants are introduced into the AlGaAs barrier layer some 50 nm away from the GaAs layer and thus spatially separated by a AlGaAs spacer layer. This reduces Coulomb scattering in the 2DEG induced by the doping and produces very high-quality samples as evidenced for example by the observation of the fractional quantum Hall effect [2]. It is hence not at all surprising that early quantum dot experiments also took place in this well-understood material system. While undoped approaches to electron and hole spin qubits in GaAs exist [3–6], they introduce added complications because of the need to electrostatically induce a 2DEG and reliably contacting it [7]. What is more, these issues are exacerbated when the structures need to be thinned down to a membrane [8, 9]. Therefore, to accommodate gate-defined quantum dots (GDQDs) next to the optically active quantum dot (OAQD) in the membrane, the devices measured in this part of the present thesis are fabricated on doped heterostructures hosting a 2DEG. In the following, I discuss the optical behavior of these structures under illumination.<sup>1</sup>

## 7.1 Photoluminescence in doped GaAs/Al<sub>x</sub>Ga<sub>1-x</sub>As heterostructures

Consider an intrinsic, direct-gap, Zincblende semiconductor such as GaAs with a band gap of  $E_g = 1.519$  eV at zero temperature [15]. At the  $\Gamma$ -point, the conduction band is well approximated by a parabolic band with effective mass  $m_c^*/m_e = 0.067$  and is offset by  $E_g/2$  above the Fermi level  $\mu$ . Offset by the same absolute amount in the opposite direction is the valence band, which close to  $\Gamma$  is fourfold degenerate with heavy and light holes with effective masses  $m_{hh}^*/m_e = 0.34$  and  $m_{lh}^*/m_e = 0.09$ , respectively [16]. The third valence band<sup>2</sup> is split off by the spin-orbit interaction and lies 0.34 eV below the other valence bands [17]. Introducing confinement in one direction, for example by doping a GaAs/Al<sub>x</sub>Ga<sub>1-x</sub>As heterojunction or growing a GaAs quantum well (QW) sandwiched between two layers of AlGaAs, lifts the fourfold degeneracy of light and heavy holes and leaves – under usual conditions – the latter as the valence band ground state.

Doping in sufficiently high concentration then raises the Fermi level from mid-gap to inside the conduction band in the plane of confinement, resulting in a band structure as sketched in Figure 7.1. The bands remain parabolic as function of the in-plane wave vector  $k_{||}$  close to  $\Gamma$ . The conduction band is filled up to  $\mu$  where, measured from the conduction band edge,  $E_c(k_{||} = k_F) = E_F = \hbar^2 k_F^2 / 2m_c^*$  with the Fermi wave vector  $k_F \sim 10^8 \text{ m}^{-1}$ . Now, absorption of a photon incident on the semiconductor demands conservation of energy and momentum. The latter condition implies that hole and electron have close to equal momentum because  $k_\gamma = 2\pi/\lambda \approx 8 \times 10^6 \text{ m}^{-1}$  is much smaller than  $k_F$ . Thus, excitation of an electron-hole pair from the valence into the conduction band occurs only for  $k \geq k_F$ . By contrast, recombination can take place for any  $k$  in principle. In practice, however, photo-electrons quickly relax down

1: The *electrical* behavior is another matter; there, illumination can lead to the creation, trapping, and de-trapping of free charge carriers that alter the transport properties of the device, leading to electrical hysteresis and instability [9–13].

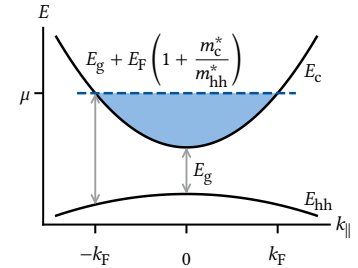


**Figure 7.1:** Band structure diagram of a doped heterostructure (after Reference 14). Due to the *n*-type doping, the conduction band is filled up to the Fermi level  $\mu$ . Photonic excitation of an electron-hole pair can only occur at  $|k| > k_F$  into the free states above  $\mu$  due to the small photon momentum. Recombination can occur within a bandwidth of  $E_F(1 + m_c^*/m_{hh}^*)$ .

2: The valence bands are *p*-like and hence contain contributions from three twofold degenerate atomic orbitals.

to the Fermi level, and recombination takes place between electrons inside the Fermi sea and photo-holes somewhere in the valence band at  $k \leq k_F$ .<sup>3</sup> The former condition then implies  $E_\gamma \geq E_g + E_F (1 + m_c^*/m_{hh}^*)$  because no free electron states are available in the conduction band below  $\mu$  due to the Pauli exclusion principle and where the term in parentheses is due to the valence band dispersion. Many-body effects due to localized photo-holes scattering with electrons of the Fermi sea can lead to a strong enhancement of luminescence intensity at the Fermi edge, the so-called Fermi-edge singularity (FES) [18–20]. The intensity of the photoluminescence (PL) at the Fermi edge relative to recombination at the band edge ( $k_{||} = 0$ ) is thus an indicator of the QW interface quality and degree of alloy fluctuations, both of which lead to hole localization [21, 22].

Free electron-hole pairs created by photo-excitation can form hydrogenic bound states due to the Coulomb attraction of their opposite electric charges, *excitons*. In two dimensions, this effect is strongly enhanced due to the increased overlap of electron and hole wave functions. Furthermore, the reduced dimensionality also enhances the binding energy from  $\sim 4$  meV in bulk GaAs to up to four times that in GaAs QWs [23, 24]. Rather than the continuum of the joint density of states of valence and conduction band discussed previously, excitons are discrete states whose energy is lower than the band gap energy by the binding energy,  $E_X = E_g - E_b$ . In doped QWs hosting a 2DEG, the free carriers can screen the exciton binding energy and lead to an ionized electron-hole plasma [25]. This is known as the insulator-to-metal (Mott) transition in semiconductors [26]. Competing with this are so-called Mahan excitons [18, 19] that give rise to the FES [27].

Next, I discuss the influence of an electric field on excitons. For this, we return to undoped structures for simplicity.

## 7.2 The quantum-confined Stark effect

Consider the electron-hole pair in bulk GaAs in the co-moving frame of the hole. The hole generates the Coulomb potential

$$V(r) = \frac{e}{4\pi\epsilon_0\epsilon_r|r|}, \quad (7.1)$$

where  $\epsilon_r = 13.3$  is the relative permittivity of GaAs at low temperatures, which attracts the electron by the Coulomb energy  $E(r) = qV(r) = -eV(r)$ . Figure 7.2 depicts the Coulomb potential in magenta and the bound electron's wave function sketched in black. The electron-hole separation  $r$  is shown in units of the exciton Bohr radius in two dimensions [28]

$$a_B = \frac{2\pi\epsilon_0\epsilon_r\hbar^2}{\mu e^2} = 6 \text{ nm} \quad (7.2)$$

with  $\mu$  the reduced effective mass of conduction and heavy-hole valence bands.

We now apply an electric field  $F$ . This modifies the potential seen by the electron by  $erF$  as sketched in green Figure 7.2. Ignoring changes to the electron wave function, we can see that the electron can tunnel out of the Coulomb potential, leading to *field-induced ionization* of the exciton. Now place the exciton in a QW instead of in bulk with the electric field pointed such that it is out-of-plane of the QW. The field still tilts the

3: For sufficiently localized states in real space, a wide range of  $k$  states in the valence band is available for recombination as states are extended in  $k$ -space. We can estimate the localization length required for states up to  $k_F$  to participate by  $\Delta x \geq 1/2\Delta k = 1/2k_F \sim 5 \text{ nm}$  for a typical 2DEG.

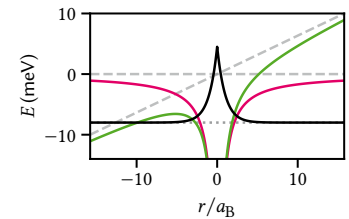


**Figure 7.2:** Effect of an in-plane electric field on an exciton wave function. In the hole's reference frame, the electron sees a static attractive Coulomb potential (magenta), resulting in a bound state (dotted gray line, wave function sketched in black). Applying an electric field ( $F = 100 \text{ mV}/\mu\text{m}$ , dashed gray lines) tilts the Coulomb potential (green) and leads to a transparent barrier through which the electron can tunnel out.

potential, but because electrons and holes are confined into a quasi-two-dimensional plane, they cannot escape and hence do not dissociate. This is the quantum-confined Stark effect (QCSE) [29].

In order to obtain a qualitative understanding of the QCSE, consider an undoped GaAs/Al<sub>0.33</sub>Ga<sub>0.66</sub>As QW of width  $L = 20$  nm. We take a 57:43 ratio for the band offsets [16], resulting in discontinuities of height  $\Delta E_c = 0.24$  eV and  $\Delta E_{hh} = 0.18$  eV at the interfaces for the conduction and the heavy-hole valence band, respectively, and  $m_c^*/m_e = 0.067$  and  $m_{hh}^*/m_e = 0.34$  for the effective masses.<sup>4</sup> Assuming an infinitely deep well for simplicity, the eigenenergies are

$$E_n = \frac{1}{2m^*} \left[ \frac{\pi \hbar n}{L} \right]^2 \quad (7.3)$$

and the eigenstates are

$$\psi_n(z) = \sqrt{\frac{2}{L}} \sin\left(\frac{n\pi z}{L}\right). \quad (7.4)$$

The ground state energy is then 14 meV (3 meV) above (below) the conduction (valence) band edge, corresponding to 6 % (2 %) of the respective band offsets and implying that the infinite-well approximation is acceptable,<sup>5</sup> while the first excited state lies 42 meV higher than the ground state. The upper panel of Figure 7.3 depicts the first two wave functions of electrons and holes in a band structure diagram. Due to the symmetry of the confining potential, the wave functions are symmetric around the center of the well.

Now, applying an out-of-plane electric field tilts the bands and pulls electrons and holes to opposite interfaces of the QW. The Hamiltonian for the electrons in this case reads [17, 30, 31]

$$H = -\frac{\hbar^2}{2m^*} \frac{d^2}{dz^2} + eFz \quad (7.5)$$

if we take  $z$  to be zero at an interface and choose  $F \geq 0$ . Introducing the length and energy scales [17]

$$\tilde{\epsilon} = \left[ \frac{(\hbar e F)^2}{2m^*} \right]^{\frac{1}{3}}, \quad (7.6)$$

$$\tilde{z} = \left[ \frac{\hbar^2}{2m^* e F} \right]^{\frac{1}{3}} = \frac{\tilde{\epsilon}}{eF}, \quad (7.7)$$

and defining

$$Z_n(z) = z/\tilde{z} - \epsilon_n/\tilde{\epsilon} \quad (7.8)$$

with  $\epsilon_n$  the eigenvalues of  $H$ , the Schrödinger equation becomes [30]

$$\frac{d^2}{dZ_n^2} \psi_n(Z_n) = Z_n \psi_n(Z_n). \quad (7.9)$$

Equation 7.9 is known as the Stokes or Airy equation and has the general solution

$$\psi_n(Z_n) = \alpha_n \text{Ai}(Z_n) + \beta_n \text{Bi}(Z_n), \quad (7.10)$$

where  $\text{Ai}(z)$  and  $\text{Bi}(z)$  are the Airy functions.  $\text{Ai}(z)$  and  $\text{Bi}(z)$  oscillate for  $z < 0$  and decay (grow) exponentially for  $z > 0$ , respectively. As we assumed infinitely high barriers at  $z = 0$  and  $z = L$ , the boundary

4: I note that the literature knows many different values for the hole effective mass in the plane of a quantum well, suggesting that one should actually measure it to be confident in the actual value.

5: In a finite well, the wave functions decay exponentially into the barriers and result in slightly lower eigenenergies. However, the qualitative behavior remains the same.

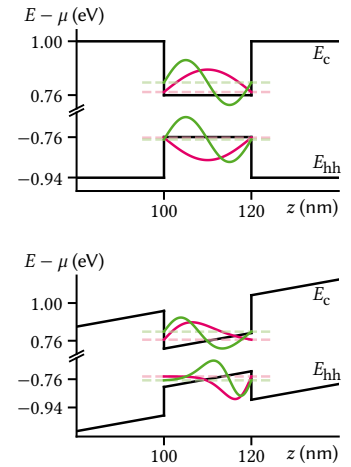


**Figure 7.3:** QCSE in an undoped QW. Top: conduction and heavy-hole valence band profiles along the growth direction. The wave functions of the first two eigenstates in the well are drawn in magenta and green, respectively. The ground state transition is larger by  $\Delta E = 17$  meV than the gap  $E_g$  due to the confinement. Bottom: same structure as above with an out-of-plane electric field applied across the structure ( $F = 5$  V/μm). Analytical wave functions in the infinite-well approximation are shown in magenta and green again. The wave functions get pushed to opposite interfaces of the QW, lowering the ground state transition energy by  $\Delta E = -10$  meV. Excitonic effects are not included.

conditions impose

$$\psi_n(Z_n(0)) = \psi_n(Z_n(L)) = 0, \quad (7.11)$$

which completely determines the eigenstates and -energies. For large well widths or fields ( $eFL/\epsilon_n \gg 1$ ), the second term is exponentially suppressed and the eigenenergies are given by the zeros of  $\text{Ai}(Z_n)$ . For zero field, one recovers the square well solution (Equations 7.3 and 7.4).

The finite-field case is shown in the lower panel of Figure 7.3 for  $F = 5 \text{ V}/\mu\text{m}$ . Due to the larger effective mass of the heavy holes, the characteristic length scale  $\tilde{z}$  is shorter and hence the corresponding wave functions are narrower than their electronic counterparts. The ground state transition energy at this field is 10 meV below the gap or 27 meV lower than in the zero-field case.

For a full quantitative accounting of the transition energies, the exciton binding energy as well as finite barrier heights would need to be included. The former is on the order of 6 meV to 9 meV in GaAs and becomes smaller as the overlap of the electron and hole wave functions is reduced when applying an electric field, pulling the wave functions to opposite interfaces [29]. Miller et al. [31] found that finite-well properties could be reproduced by using effective well widths with infinite-well models. The latter should have a small effect on the ground state energy as argued above.

### 7.2.1 In-plane confinement

So far, we have considered the QCSE in a single dimension, as if we were to apply a global electric field. However, as we saw before, the field lowers the exciton energy below the QW confinement and hence, if applied locally, results in an effective confinement potential in the plane of the QW. Descamps [8] performed numerical simulations for a geometry with circular gate electrodes with 200 nm diameter on both sides of a membrane, finding a confinement depth of  $V_0 = 20 \text{ meV}$  at  $F = 5 \text{ V}/\mu\text{m}$  that is well approximated by a single-particle harmonic potential for the center-of-mass wave function of the exciton,  $V(\rho) = M\omega^2\rho^2/2 - V_0$ , with mass  $M = m_c^* + m_{hh}^*$  and confinement strength  $\omega/2\pi = 738 \text{ GHz}$  corresponding to an oscillator length  $\xi = \sqrt{\hbar/M\omega} = 20 \text{ nm}$ . To obtain a qualitative picture, let us interpolate this result for different fields. The depth of confinement corresponds to the energy shift induced by the QCSE and is quadratic in  $F$ ,  $V_0 = -\alpha F^2$ . At vanishing field, there should be no in-plane potential,  $\omega = 0$ . Hence, we can assume that  $\omega \propto F$  to leading order and thus  $V(\rho) = \beta MF^2\rho^2/2 - \alpha F^2$ .

How does this in-plane confinement modify the wave function? We ignore the relative motion of electron and hole as the optical properties of the exciton are dominated by the behavior at zero separation for  $a_B/\xi < 1$  [32], and consider only  $\Delta n = 0$  transitions, *i.e.*, electron and hole in the same  $z$  quantum state, as  $\Delta n \neq 0$  transitions are much weaker [17]. Let us further initially assume a separable wave function and choose cylindrical coordinates according to the symmetry of the potential. We then have

$$\Psi_{npl}(z_e, z_h, \rho, \phi) = \psi_n(z_e)\psi_n(z_h)\chi_{pl}(\rho)\exp(i\ell\phi) \quad (7.12)$$

where<sup>6</sup> [33]

6: Note that Karimi et al. miss a factor  $2\pi$  in the normalization.

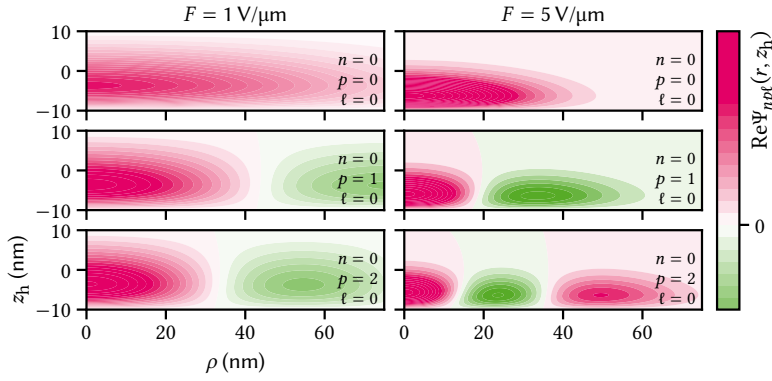


**Figure 7.4:** Center-of-mass exciton wave function (hole sector) in a harmonic trap under an electric field. Left column shows the low-field and right column the high-field case. Top row is the ground state, middle and bottom row the first and second excited state in the plane, respectively. The out-of-plane wave function is the ground state in all cases ( $n = 0$ ) and the trap confinement strength  $\omega/2\pi = 738$  GHz for  $F = 5$  V/ $\mu\text{m}$  [8, Section 2.2.2] and linearly interpolated for 1 V/ $\mu\text{m}$  (see text).

$$\chi_{p\ell}(\rho, \phi) = \sqrt{\frac{2p!}{2\pi\xi^2(p+|\ell|)!}} \exp(-\tilde{\rho}^2/2) \tilde{\rho}^{|\ell|} L_p^{|\ell|}(\tilde{\rho}) \quad (7.13)$$

with the associated Laguerre polynomial  $L_p^{|\ell|}(x)$  and we used the shorthand  $\tilde{\rho} = \rho/\xi$ . The numbers  $p \in \mathbb{N}$  and  $\ell \in \mathbb{Z}$  denote the principal and orbital momentum quantum numbers. The eigenenergies of the harmonic oscillator solution, Equation 7.13, are given by

$$\epsilon_{p\ell} = \hbar\omega(2p + |\ell| + 1). \quad (7.14)$$

To account for a finite well width ( $L \approx \xi$  in our case), we can to a first approximation perform the replacement  $\rho \rightarrow r = \sqrt{\rho^2 + z^2}$  in Equation 7.12. The resulting wave function  $\Psi_{npt}(r, z_h)$  at fixed electron coordinate  $z_e$  is shown in Figure 7.4 for  $n = \ell = 0$  (which makes it independent of  $\phi$ ).  $\Psi_{npt}$  has  $n$  nodes along  $z$  and  $p$  nodes along  $\rho$  for  $\ell = 0$  as we would expect.

At last, we can use the exciton wave function  $\Psi_{nmt}(r, \phi, z_e, z_h)$  to estimate the *oscillator strength*, a quantity often quoted in semiconductor spectroscopy. The oscillator strength puts in relation the quantum mechanical transition rate with the emission rate of a classical oscillator with frequency  $\omega = \Delta E/\hbar$  matching the transition energy [34]. For a dipole transition from state  $|i\rangle$  to state  $|j\rangle$ , it may be written as [17]

$$f_{ji} = \frac{2\mu\Delta E_{ji}}{\hbar^2} |\langle j|\mathbf{r}|i\rangle|^2, \quad (7.15)$$

where  $\mu$  is the reduced mass of the exciton. As the selection rules only allow in-plane dipole transitions for heavy holes, we write [32]

$$f_{npt} = \frac{2\mu\epsilon_{npt}}{\hbar^2} J_r^2 J_\phi^2 |\langle u_c|x|u_{hh}\rangle|^2 \quad (7.16)$$

for transitions with  $\Delta n = \Delta p = \Delta \ell = 0$ , where

$$J_r = \int_0^L dz \int_0^\infty d\rho \rho \psi_n^{(e)}(z) \psi_n^{(h)}(z) \chi_{p\ell}(\sqrt{\rho^2 + z^2}), \quad (7.16a)$$

$$J_\phi = \int_0^{2\pi} d\phi \exp(i\ell\phi), \quad (7.16b)$$

$$\epsilon_{npt} = \epsilon_n + \epsilon_{p\ell}, \quad (7.16c)$$

and  $|u_{c(hh)}\rangle$  are the Bloch functions of the valence and conduction band, respectively, that we have neglected so far. From Equation 7.16b, we immediately see that the oscillator strength of states with nonzero orbital



momentum ( $\ell \neq 0$ ) vanishes,  $f_{np0} = 0$ ! This in turn implies from Equation 7.14 that the exciton level spacing in a radially symmetric trap is given by  $\Delta E = 2\hbar\omega = 1 \text{ meV}$ , a factor of two larger than assumed by Descamps [8].

As we tilt the bands, energy levels below the QW become available in the barrier once  $\Delta E_{c(\text{hh})} - \epsilon_n \sim eFd$  with  $d$  the width of the barrier. This allows confined carriers to escape the QW with a finite probability by tunneling through the barrier, an effect known as Fowler-Nordheim tunneling. Following Reference 17, we can estimate the tunneling probability as<sup>7</sup>

$$\mathcal{T}_n(F) \approx \exp \left\{ -\sqrt{\frac{4m^*[\Delta E_{c(\text{hh})} - \epsilon_n]^3}{eF\hbar}} \right\}. \quad (7.17)$$

The tunneling rate  $\Gamma_n$  can then be estimated by the frequency that a confined charge carrier “visits” the edge of the QW multiplied by the probability that it tunnels,  $\mathcal{T}_n$  [35]. That is, we take  $\epsilon_n$  to be a kinetic energy and calculate the velocity as

$$v_n = \frac{\hbar k_n}{m_{c(\text{hh})}^*} = \sqrt{\frac{2\epsilon_n}{m_{c(\text{hh})}^*}}. \quad (7.18)$$

Then the frequency of one round trip inside the QW is

$$\tau_n^{-1} = \frac{v_n}{2L} = \frac{1}{L} \sqrt{\frac{\epsilon_n}{2m_{c(\text{hh})}^*}} \quad (7.19)$$

and

$$\Gamma_n = \frac{\mathcal{T}_n}{\tau_n}. \quad (7.20)$$

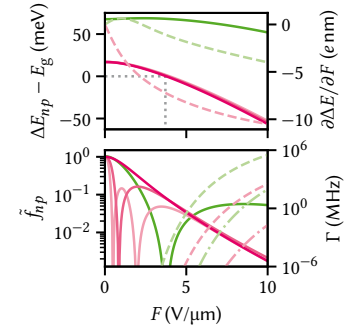
What is the order of magnitude of  $\tau_n$ ? For an energy of  $\epsilon_n = 10 \text{ meV}$ ,  $\tau_n \approx 200 \text{ fs}$  for electrons and  $400 \text{ fs}$  for holes. The tunneling probability  $\mathcal{T}_n$  therefore needs to be quite small indeed for the rate  $\Gamma_n$  to remain small.

Figure 7.5 summarizes the QCSE in a QW additionally confined in the plane by local electric fields. The top panel shows the exciton transition energy  $\Delta E_{np}$  for  $\Delta n = \Delta p = 0$  in solid lines.<sup>8</sup> The first three in-plane sublevels due to the harmonic potential are drawn in less saturated colors but hard to see because the level spacing is much smaller than the out-of-plane QW subband spacing,  $\sim 1 \text{ meV}/50 \text{ meV}$ . The ground state shows the expected quadratic dependence on the electric field also obtained, for example, from perturbation theory. Drawn as a dashed line is the induced dipole moment,

$$\mathbf{p}_{np}(F) = \frac{\partial \Delta E_{np}}{\partial F} \hat{\mathbf{e}}_z, \quad (7.21)$$

which is monotonously decreasing for the ground state as function of electric field  $F$ , consistent with a continuous lowering of energy. For the first excited state, the induced dipole moment is actually positive below  $2 \text{ V}/\mu\text{m}$ , leading to a repulsive interaction and hence a raising of the transition energy by up to  $1 \text{ meV}$ . The lower panel shows the oscillator strength, Equation 7.16, normalized to its value of the ground state at zero field,  $f_{00}(F = 0)$ . For the ground state it decays exponentially with the electric field as the overlap between electron and hole wave functions, which decay exponentially into the QW themselves, is reduced.  $f_{0p}$  for

7: The same result up to a slightly different numerical prefactor in the exponent is obtained more formally from the WKB approximation [8].



**Figure 7.5:** Electric field dependence of the QCSE for the first two energy levels in the QW. Top: the ground state energy (magenta) shows the expected quadratic dependence; the confinement energy is compensated at around  $F = 3.7 \text{ V}/\mu\text{m}$ . Higher in-plane orbital levels are shown for the QW ground state in decreasing saturation. For zero field, the splitting is zero as there is no in-plane confinement. At maximum field, the splitting is  $2\hbar\omega = 2 \text{ meV}$ . Dashed lines (right axis) show the derivative, revealing that the QW excited state is actually raised in energy at low fields. Bottom: oscillator strengths (same color code as above). Dashed lines (right axis) show the electron tunneling rate through the barrier, dash-dotted the holes.

8: Note again that we neglected the exciton binding energy, which decreases



higher in-plane orbital states ( $p > 0$ , magenta, decreasing saturation) has an envelope following the ground state's exponential decay but vanishes at  $p$  points in  $F$  due to the fact that the wave function has  $p$  nodes. By contrast,  $f_{10}$  for the first excited QW state (green) does not decay to zero at large fields but also has a zero at an intermediate field because of the wave function's node along  $z$ .

Finally, the right axis shows the estimated tunneling rates (Equation 7.20) of the electron (hole) ground (excited) states in dashed (dash-dotted) magenta (green) lines, respectively. Rates of electrons are at least four orders of magnitude larger than those of holes owing to their smaller effective mass despite the larger band offset. At  $F = 5 \text{ V}/\mu\text{m}$  corresponding to a voltage of 1 V across a membrane of 200 nm thickness, the electron tunnel rate is on the order of 1 Hz, but rises very quickly above that. Considering once again a QW hosting a 2DEG and neglecting associated band bending effects, this rate corresponds to a current through a circular area of  $1 \mu\text{m}$  in diameter of 600 aA at an electron density of  $n = 5 \times 10^{11} \text{ cm}^{-2}$ , but already 600 pA at  $7.5 \text{ V}/\mu\text{m}$ .

### 7.3 Excitonic complexes

If we liken the exciton to a Hydrogen atom<sup>9</sup> with modified binding energy  $E_b$  and Bohr radius  $a_B$ , it is natural to expect molecules and ions of these states to exist. The simplest molecule, or excitonic complex, is the biexciton, the analog of the  $\text{H}_2$  molecule. Following a similar argument as for the binding energy of the exciton, we expect that of the biexciton to also increase as the dimensionality of the system is reduced. Indeed, in QWs it has been measured to be on the order of 1 meV, 3 to 4 times larger than in 3D [36], although also negative binding energies, corresponding to an anti-bonding state, have been reported [37–39]. A signature of biexcitons is the power dependence of their PL. The steady-state density of electron-hole pairs, which is proportional to the exciton density at low enough powers, is proportional to the irradiance, *i.e.*, the excitation power. Conversely, the probability to form a two-body bound state is proportional to the square of the density of those bodies and we hence expect the power under the PL peak of a biexciton emission to be proportional to the square of the laser power used to excite the sample.

Besides the neutral biexciton, there exist also charged states consisting of three or more bodies. Here, additional electrons or holes bind to an exciton, forming negative or positively charged trions similar to  $\text{H}^-$  or  $\text{He}^+$  ions. Naturally, this process is favored when a large number of surplus charge carriers is present in the sample such as is the case in doped QWs with a 2DEG (or two-dimensional hole gas (2DHG)) [40]. In these structures, the trion binding energy has been found to also be on the order of 1 meV [41, 42].

9: Although positronium is a better analogon.

# The mjolnir measurement framework

8

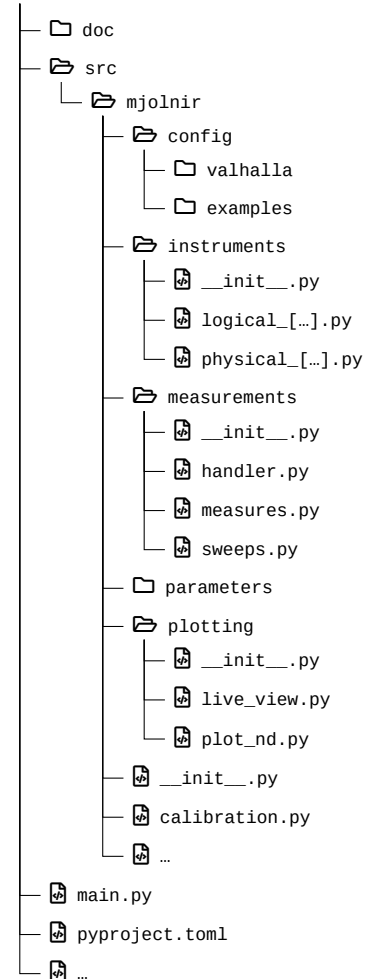


**Figure 8.1:** Source tree structure of the mjolnir package. Logical QCoDeS instruments and parameters are defined in the instruments and parameters modules, respectively. Instruments are configured using yaml files located in a config subdirectory. The measurements module provides classes for the abstraction of measurements using QCoDeS underneath. Live plots of instrument data as well as a plot function for multidimensional measurement data are defined in the plotting module. calibration.py contains routines for power, CCD, and excitation rejection calibrations. The main.py file is a code cell-based script that serves as the entrypoint for measurements.

In this chapter, I present and discuss optical measurements of gated semiconductor membranes. All of the samples under investigation here had the same nominal heterostructure layout; a 20 nm GaAs QW sandwiched between two modulation-doped 90 nm  $\text{Al}_{0.33}\text{Ga}_{0.67}\text{As}$  barriers of which 50 nm are an undoped spacer layer. Together with a 5 nm or 10 nm GaAs cap to on both sides to protect the Aluminium from oxidation, the membranes had a thickness of 210 nm or 220 nm after thinning.

Gate electrodes are patterned on the top and bottom side of the membrane using electron-beam lithography (EBL), where here and elsewhere in the present thesis I refer by “top” to gates on the etched and by “bottom” to those on the grown surface. That is, “top” gates are on the air side when the sample is mounted in the fridge, whereas “bottom” gates are in contact with the epoxy glueing them to the Silicon host chip. Typical designs have gates on the top and bottom sides of the membrane start at different positions on the mesa and converge towards the exciton trap site, where they overlap laterally. For details about the fabrication process, refer to References 8 and 9.

I installed the samples in the dilution refrigerator (DR) introduced in Part II and cooled them to Millikelvin temperatures. As detailed there, PL measurements can be performed by illuminating the sample with a continuous-wave (cw) laser above the band gap through an objective lens in front of the sample. The emitted PL radiation is picked up by the same lens and coupled into a single-mode fiber (SMF) outside the fridge, from where it is sent to a diffraction grating spectrometer with a charge-coupled device (CCD) for spectral analysis.

In total, I show measurements from three different samples. Unfortunately, none of the samples tested had a fully functional exciton trap with four working gates. Several old samples fabricated during the work of Descamps [8] appeared to have aged, resulting in broken gates or otherwise unconventional behavior. Newly fabricated samples on old heterostructure pieces frequently showed contact problems, either of optical gates to the mesa, between different EBL resolution steps, or Ohmics, while other gates had leakage to ground or the QW.

I pursued two different approaches to positioning the laser on the samples. The first was using the white-light imaging arm of the confocal microscope (see Part II). The larger gate structures on the samples typically show good contrast in the complementary metal-oxide-semiconductor (CMOS) camera image, allowing orientating oneself following the sample design. However, the simplicity of the optics<sup>1</sup> results in a comparably poor contrast for the smallest features on the scale below 1  $\mu\text{m}$ . The magnification factor of the microscope is 30, resulting in a feature size of 160 nm per pixel on the camera. In the best-case scenario, the cryostat vibration noise is on the order of 100 nm root mean square (RMS) (Section 4.3), or roughly one pixel. Resolving features only a few pixels in size is thus clearly on the edge of the microscope’s capabilities. Positioning the sample in this way is usually fairly reliable with some experience if one takes visual identification of the exciton trap gates as a target. In practice, it is still necessary to fine-tune the position once the light source is switched to the laser because first, the focal distance of the objective lens shifts slightly when switching from a broadband to

1: The objective is just a singlet lens, compared to sophisticated commercial objectives containing a large number of optics inside to correct optical aberrations. See for example the [Attocube LT-APO/LWD](#).

a monochromatic light source, and second, the focal spot of the laser is much smaller than that of the white light.<sup>2</sup>

The second approach is to roughly align the position on a large gate feature using the camera image, switch to laser illumination, and monitor the PL signal when biasing the gate. One can then move along the gate towards the exciton trap by following the PL features expected for a gate: a reduced QW emission due to absorption (see Section 9.3) and enhanced reflection of the laser line, as well as a Stark-shifted PL. This has the advantage that the functionality of the gate can be monitored. Biasing also the other gates of the trap under investigation one can then look for additional Stark shifting of the PL. If the effect of each gate voltage can be observed, the position of the laser will be close to the trap center, and can then be optimized further. While this is in a sense flying in the dark, it is a quite reliable method for an experienced experimentalist *if* the gates are fully functional.

## 9.1 Photoluminescence spectroscopy

Figure 9.1 shows a typical PL spectrum obtained on the bare, unbiased QW of a doped membrane sample. This measurement corresponds to the configuration already discussed in Section 7.1. Due to the Pauli exclusion principle, electrons require an energy of at least  $E_F (1 + m_c^*/m_{hh}^*)$  above the band gap and, because of the vanishingly small photon momentum, a momentum of at least  $k_F$  to be excited into a free state above the Fermi level  $\mu$  (dotted gray line).<sup>3</sup> Once excited, they quickly relax down to the Fermi edge at  $\mu$  from where they can recombine emitting a photon. As the Fermi sea is at a finite temperature, the high-energy shoulder of the PL spectrum is hence thermally broadened according to the Fermi distribution function of the electron gas (dashed gray line). The associated temperature is around 1.5 K and hence orders of magnitude higher than the lattice temperature of 10 mK. This effect has already been observed by Pinczuk et al. [45]. Like in those experiments, the temperature of the Fermi edge does not vary significantly with excitation power, making carrier heating due to high excitation power an unlikely cause [46].

PL emission is possible also at lower energies as electrons inside the Fermi sea recombine with the free photo-hole that scatters towards the valence band edge. The band gap then defines the low-energy shoulder of the PL spectrum, below which there are – ideally – no states available (dotted gray line). However, the PL reveals there are indeed free states decaying exponentially into the gap, originating most likely from impurities (dashed gray line). Compared to the results of Kamburov et al. [14], the PL spectra obtained here are much flatter over energy, with the PL peak typically close to the middle between gap and Fermi edge. Conversely, Kamburov et al. [14] observed a strong peak at the band gap,<sup>4</sup> indicating that in our samples holes are more strongly localized and therefore have a wider spread in  $k$ -space, enabling transitions in a wider range of wave vectors [20]. This would in turn imply increased alloy disorder or interface roughness [22], an observation we shall come back to in Section 9.2.

From the width of the 2DEG emission, we can calculate the charge carrier density by relating it to the Fermi energy in two dimensions [1, 45],

$$n = \frac{m_c^* E_F}{\pi \hbar^2} = \frac{\mu \Delta E}{\pi \hbar^2}, \quad (9.1)$$

2: The white light is launched from a 400  $\mu\text{m}$  diameter multi-mode fiber (MMF) and collimated by a 0.13 numerical aperture (NA) lens, compared to a 5  $\mu\text{m}$  diameter SMF collimated by a 0.18 NA lens for the laser.

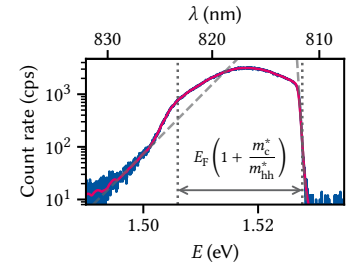


**Figure 9.1:** PL of the bare 2DEG. Magenta line is a smoothing spline fit to the data. Indicated by dotted gray lines are the Fermi edge at high and the band edge at low energy. The Fermi edge has a Fermi distribution (exponential indicated by a dashed gray line) whose temperature is typically much higher than the lattice temperature ( $\sim 1$  K). Below the band edge there is an exponential tail (dashed gray line) due to impurities that permeates far into the gap.

3: This is known as the Burstein-Moss shift [43, 44].

4: Cf. also Gabbay et al. [22], who observe all but no FES in samples nominally comparable to ours.

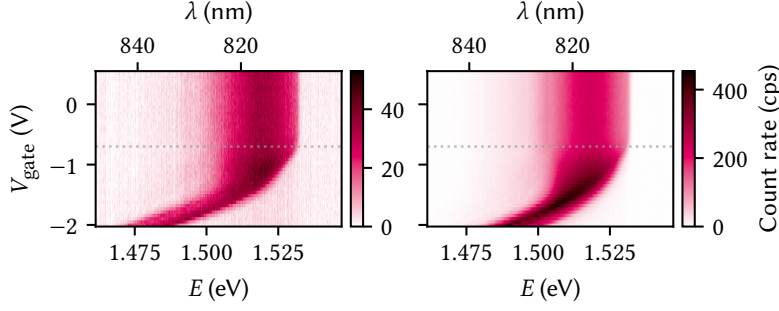


**Figure 9.2:** PL as function of gate voltage on a single fan-out gate on the bottom (left) and top (right) side of the membrane. The behavior is qualitatively similar but the overall quantum efficiency lower by an order of magnitude for gates on the bottom (as-grown buried) side. Dotted gray lines are a guide to the eye demonstrating that the changes to the PL spectrum set in at the same voltage for both types of gates (around  $-0.7$  V).

where  $\Delta E$  is the bandwidth of the emission (dashed gray lines in Figure 9.1) and  $\mu = m_c^* m_{hh}^* / (m_c^* + m_{hh}^*)$  is the reduced mass of conduction and valence band. For this particular sample, Equation 9.1 yields  $n = 5 \times 10^{11} \text{ cm}^{-2}$  or, equivalently,  $E_F = 18 \text{ meV}$  and  $k_F = 1.8 \times 10^8 \text{ m}^{-1}$ . Comparing this value to that obtained from a simulation of the heterostructure with nominal doping concentration  $N_d = 6.5 \times 10^{17} \text{ cm}^{-3}$  using a self-consistent Poisson-Schrödinger solver [47],  $n = 1.9 \times 10^{11} \text{ cm}^{-2}$ , shows a significant discrepancy indicating a severe mismatch between nominal and actual doping concentrations.<sup>5</sup> Finally, we observe that the gap according to the preceding analysis is redshifted from the undoped bulk gap of  $1.519 \text{ eV}$  [15] by  $13 \text{ meV}$ .<sup>6</sup> Descamps [8] hypothesized that the removal of the GaAs substrate and the associated change in strain leads to this lowering of the band gap. However, this effect was also already observed by Pinczuk et al. [45] in “bulk” modulation-doped GaAs QWs. There, the authors put forth a renormalization of the band gap due to many-body interactions as an explanation. Indeed, it is likely just bandgap narrowing due to doping [48].

### 9.1.1 Quantum-confined Stark shift

Let us now address the behavior of the PL under electric fields. To this end, the laser is positioned on an EBL-written gate and a negative voltage is applied to the gate. Figure 9.2 depicts measurements on a well-behaved sample. The left (right) panel shows the PL as function of voltage with the laser positioned on a bottom (top) gate. In contrast to the intuition obtained in Section 7.2, there is no immediate effect to be observed once the voltage is switched on. This is most likely due to the presence of the 2DEG screening the external electric field. At  $V_{\text{gate}} = -0.7 \text{ V}$ , the high-energy shoulder of the emission starts to shift towards lower energies while the low-energy shoulder stays invariant. Per the previous section, we can interpret this as the Fermi energy and thereby the charge carrier density being lowered as the 2DEG is depleted. As the electric field tilts the bands, the band edges of both conduction and valence band move in sync and therefore the band gap is not modified in this regime.<sup>7</sup> As the 2DEG is gradually depleted, a broad exciton peak emerges that shifts approximately quadratically with the applied voltage as ionization from the interaction with the Fermi sea of electrons becomes less (*cf.* Section 7.1). Beyond  $-1.5 \text{ V}$ , the 2DEG is completely depleted. The voltage difference between onset and completion of the depletion matches roughly the value expected from a simulation without screening for the nominal device parameters (see Tables D.1 and D.2),  $-0.7 \text{ V}$ .

Besides the voltage dependence, another feature stands out from Figure 9.2: the PL intensity is lower by an order of magnitude when on

5: Note that the carrier density obtained thus does not vary significantly with excitation power, ruling out photo-doping as a source of the discrepancy. See Appendix D for a measurement of the 2DEG PL as function of power.

6: The redshift is in fact larger still due to the confinement energy of the QW, estimated to be  $17 \text{ meV}$  in Section 7.2.

7: We would in fact expect a slight increase in confinement energy as the carrier density is lowered because the band bending due to the surplus electric charge of the 2DEG is lifted.

top of a back gate compared to a top gate. This is at first puzzling, as in the latter case there is an additional semi-transparent gate<sup>8</sup> absorbing and reflecting both laser and PL radiation, whereas in the former there is only the bare heterostructure, so we would expect the exact opposite! I elucidate this issue in Section 9.3.

Moving to a large exciton trap with a single set of top and bottom gates,<sup>9</sup> we can measure the behavior of the Stark shift in the intended setting of local confining gates on either side of the membrane. We define the virtual gates

$$V_{\text{DM}} = V_{\text{T}} - V_{\text{B}}, \quad (9.2)$$

$$V_{\text{CM}} = V_{\text{T}} + V_{\text{B}}, \quad (9.3)$$

where DM (CM) stands for difference (common) mode and T (B) for top and bottom. Clearly,  $V_{\text{DM}}$  should ideally be proportional to the out-of-plane electric field across the membrane,  $V_{\text{DM}} = Ft$  with  $t$  the membrane thickness, whereas  $V_{\text{CM}}$  should tune the band edge offset from the Fermi level  $\mu$ . As we observed previously, the presence of the 2DEG screens the electric field generated by  $V_{\text{DM}}$ . A good operating point is therefore at a negative  $V_{\text{CM}}$  which should deplete the 2DEG (or at least reduce the charge carrier density). Figure 9.3 shows a PL map as function of the difference mode voltage  $V_{\text{DM}}$  at  $V_{\text{CM}} = -1.3$  V. From Figure 9.2, where the optical measurement of the charge carrier density results in a similar value as for the sample in Figure 9.3,  $n \sim 5 \times 10^{11} \text{ cm}^{-2}$ , we would expect this common mode voltage to suffice in at least overcoming the screening and reducing the carrier density in the QW. However, there is clearly still a 2DEG emission present for a large range of  $V_{\text{DM}}$ , and the Fermi edge is at the same energy as without a gate bias. Overall, the Stark shift pattern is symmetric but offset by  $V_{\text{DM}} = 0.75$  V. This behavior is also observed in the response of the PL to a single gate in this and several other samples, where the onset of an effect by bottom gate is significantly later than that for the top gate, suggesting that the voltage is screened by some mechanism. Perhaps surprisingly, the gates on the *bottom* side of the membrane display this behavior, *i.e.*, the gates on the as-grown surface.<sup>10</sup> This makes surface states an unlikely candidate for the screening as the quality of the grown surface should be better than that of the etched surface [8]. A possible cause might be oxygen segregation during growth\* or other impurities [50].

The fact that the 2DEG is depleted by  $V_{\text{DM}}$  in the range  $-0.2$  V to  $-1.4$  V and above  $1.5$  V at all is unexpected. Even with an offset as just discussed, the symmetric dependence of the PL emission on  $V_{\text{DM}}$  implies that the lever arms of both gates are comparable and hence  $V_{\text{DM}} - 0.75$  V *should* correspond to the out-of-plane electric field such that the energy is unchanged in the middle of the quantum well,  $V_{\text{DM}} - 0.75 \text{ V} \propto F(z - t/2)$ . In and of itself, this parameter should not reduce the charge carrier density in an isolated QW to first order.<sup>11</sup> One possible explanation for the observed behavior is the depletion of the 2DEG by electrons tunneling out of the well and recombining with the donor ions, rendering one of the doped barriers electrically neutral. With the doping pulling down the conduction band between  $50$  nm and  $90$  nm away from the QW, the tunneling rate will be more pronounced than estimated for the undoped case in Section 7.2. Taking the large trap diameter in this case into account, there are  $\sim 10^5$  electrons in the unbiased QW on the area of the trap gates. Thus, at a tunneling rate of  $1$  MHz, all electrons would tunnel out of the QW within  $100$  ms on average, putting a response of the

8: 7 nm Au with a 2 nm Ti adhesion layer.

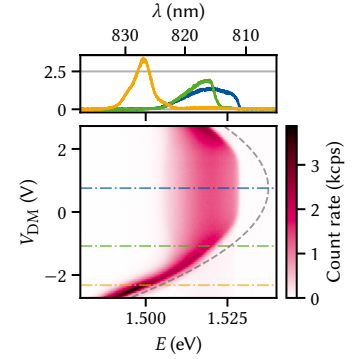


**Figure 9.3:** PL as function of difference-mode voltage on a large exciton trap. The observed Stark shift follows roughly the expected quadratic dispersion, but is offset by  $0.75$  V with respect to zero bias. Dashed gray line is a guide to the eye of a parabola with curvature  $-3.5 \text{ meV/V}^2$ . Line cuts in the upper panel are taken at the voltages indicated by dash-dotted lines in the lower.

9:  $5 \mu\text{m}$  diameter.

10: I note that the sample of Figure 9.2 was fabricated on the same heterostructure as the device in Figure 4(d) of Reference 49, which showed little to no electrical hysteresis unlike most other samples investigated by Descamps [8].

11: We might instead expect a small change in the apparent gap energy as the well is tilted.

\* A. Ludwig, private communication.



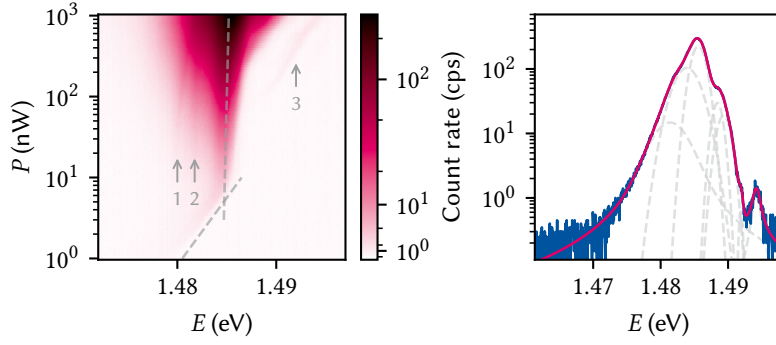


**Figure 9.4:** PL as function of excitation power  $P$ . In the left panel two qualitatively different regimes are indicated by dashed gray lines as guides to the eye; below 10 nW, the main peak displays a blueshift logarithmic in excitation power,  $E = 1.485 \text{ eV} + 5 \text{ meV} \log_{10} P$ . Above, the blueshift diminishes significantly. Three additional lines, indicated by arrows, with varying power dispersion are visible. Right panel shows a fit to data at  $P = 1 \mu\text{W}$ . A sum of seven individual lines (dashed, gray) is required to fit the data. The dashed gray lines are the individual contributions.

system into the steady state within the fairly long time scales of a PL measurement<sup>12</sup> well within reasonable bounds. In the literature, this is known as carrier sweep-out and has been studied in the context of solar cells and other electroabsorptive devices [35, 51, 52].

The dashed gray line in Figure 9.3 shows a parabola as a guide to the eye. For difference-mode voltages below  $-1.8 \text{ V}$ , the exciton Stark shift follows this quite closely. The upper panel depicts three line cuts at the positions indicated by the dash-dotted lines in the main panel. As can be seen from the cut at  $-2.3 \text{ V}$  (orange), the line shape appears to consist of distinct emission lines assigned by Descamps [8] as the neutral, singly, and doubly negatively charged excitons. I return to the question of line assignment in Section 9.2.

### 9.1.2 Power dependence

As outlined in Section 7.3, the dependence of emitted PL power on excitation power of individual emission lines can help inferring the excitonic species responsible. Moreover, as the density of excitons depends on the excitation power, interaction effects between them influence the energy of the emission. Such a measurement is shown in the left panel of Figure 9.4 for the same common-mode voltage as in Figure 9.3 and  $V_{\text{DM}} = -2.7 \text{ V}$  (*i.e.*, corresponding to the lowest line in that plot) where the 2DEG is completely depleted. Two qualitatively different regimes can be observed as indicated by the dashed gray lines as guides to the eye. Below 10 nW excitation power, corresponding to approximately  $0.75 \text{ W/cm}^2$  at the beam diameter measured in Part II, the main line displays a blueshift logarithmic in excitation power. Above this value, the blueshift is much less pronounced. At powers above 10 nW, two additional lines on the low-energy side of the main peak become visible that appear to converge towards higher powers, while above 100 nW a line appears on the high-energy side that has a similar blueshift as the main peak at low powers. In principle, the blueshift as function of power is to be expected. Increasing the excitation power increases the density of excitons, either because they are spatially localized or confined or because of a finite diffusion speed. The increased density corresponds to an increased overlap of single exciton's constituents and thus in turn leads to an increasingly repulsive Coulomb interaction that raises their energy.<sup>13</sup> This mechanism underpins the use of exciton traps such as self-assembled quantum dots (SAQDs) as single-photon sources; upon spectrally filtering on the emission wavelength of a single exciton, only a single photon can be emitted from the trap at a time since the presence of another exciton in the trap would shift the emission energy of both. It

12: Say 0.1 s to 10 s.

13: Of course, the opposite – an attractive interaction – is also possible for small numbers of excitons, resulting in biexcitons. The two cases can be thought of analogously as bonding and anti-bonding orbital configurations.

is not understood though why the blueshift abruptly changes in quality at 10 nW excitation power.

The right panel shows a line cut taken at 1  $\mu$ W. A weighted sum of seven individual Voigt profile line shapes [53],

$$V(E; \sigma, \gamma) = G(E; \sigma) * L(E; \gamma), \quad (9.4)$$

that is, a convolution of Gaussian and Lorentzian line shapes given by

$$G(x; \sigma) = \frac{1}{\sigma\sqrt{2\pi}} \exp\left(-\frac{x^2}{2\sigma^2}\right), \quad (9.4a)$$

$$L(x; \gamma) = \frac{1}{\pi} \frac{\gamma}{\gamma^2 + x^2}, \quad (9.4b)$$

is required to obtain an adequate fit. The Voigt profile arises from a combination of two separate line broadening mechanisms that manifest as a Gaussian (Equation 9.4a) and Lorentzian (Equation 9.4b) line shape. The former describes inhomogeneous broadening due to noise faster than the data acquisition time, whereas the latter is the homogeneous broadening due to for example the finite lifetime of the emitting state.<sup>14</sup> All but the two outermost lines in the best fit are dominated by the inhomogeneous, Gaussian contribution to Equation 9.4 with widths  $\sigma$  in the range of 0.1 meV to 1 meV and a peak separation on the order of 2 meV. According to Reference 8, the lifetime of a Stark-shifted exciton is on the order of 1 ns due to the reduced wave function overlap. This corresponds to a homogeneous linewidth of  $2\gamma = \hbar/\tau \sim 660$  neV, several orders of magnitude below the observed linewidth, and it is thus consistent with the fact that most peaks are best fit by inhomogeneously broadened line shapes. The large a number of lines is certainly unexpected and cannot be explained by different excitonic species. Where it is possible to track individual peaks as function of excitation power, their power dependence is linear,  $\int dE V(E) \propto P$ , suggesting neutral excitons or band-to-band recombination as origins of the emission.

14: This is also known as the linewidth's transform limit; energy and (life)time are Fourier pairs by Heisenberg's uncertainty principle.

A possible explanation for the multitude of lines is thus that they originate from different spatial locations, a hypothesis we return to in Subsection 9.1.3. First, let us conclude this section with a large parameter sweep of this trap, shown in Figure 9.5. Each of the three rows (with separate panels for line cuts each) show data for different excitation wavelengths,  $\lambda_{\text{exc}}$ , each of the columns show data for different top gate voltage,  $V_{\text{T}}$ , and the PL is plotted as function of detection energy,  $E_{\text{det}}$ , and excitation power,  $P_{\text{exc}}$ . The line cuts taken at lower powers (blue and green) are scaled to match the one at the highest power (orange) assuming a linear power dependence. For all data  $V_{\text{B}} = 0$  V so that  $V_{\text{T}} = V_{\text{DM}} = V_{\text{CM}}$ . Despite the comparatively small changes in voltage, the behavior of the sample changes significantly. Whereas for  $V_{\text{T}} = -2.08$  V the observed PL features are similar to those in Figure D.1, at  $V_{\text{T}} = -1.92$  V there is a very large number of lines in the spectrum, most but not all of which share the same blueshift as function of excitation power. The effect of a different excitation wavelength appears to mostly be a shift of the features along the excitation power axis and thus simply a change in absorption efficiency, although some features also change qualitatively. I discuss the wavelength dependence in more detail in Section 9.2.

So what is the origin of the substructure of the PL emission? The peak distance is on the order of 1 meV. This value matches fairly closely the order of magnitude of change in ground state energy, 900  $\mu$ eV, we would



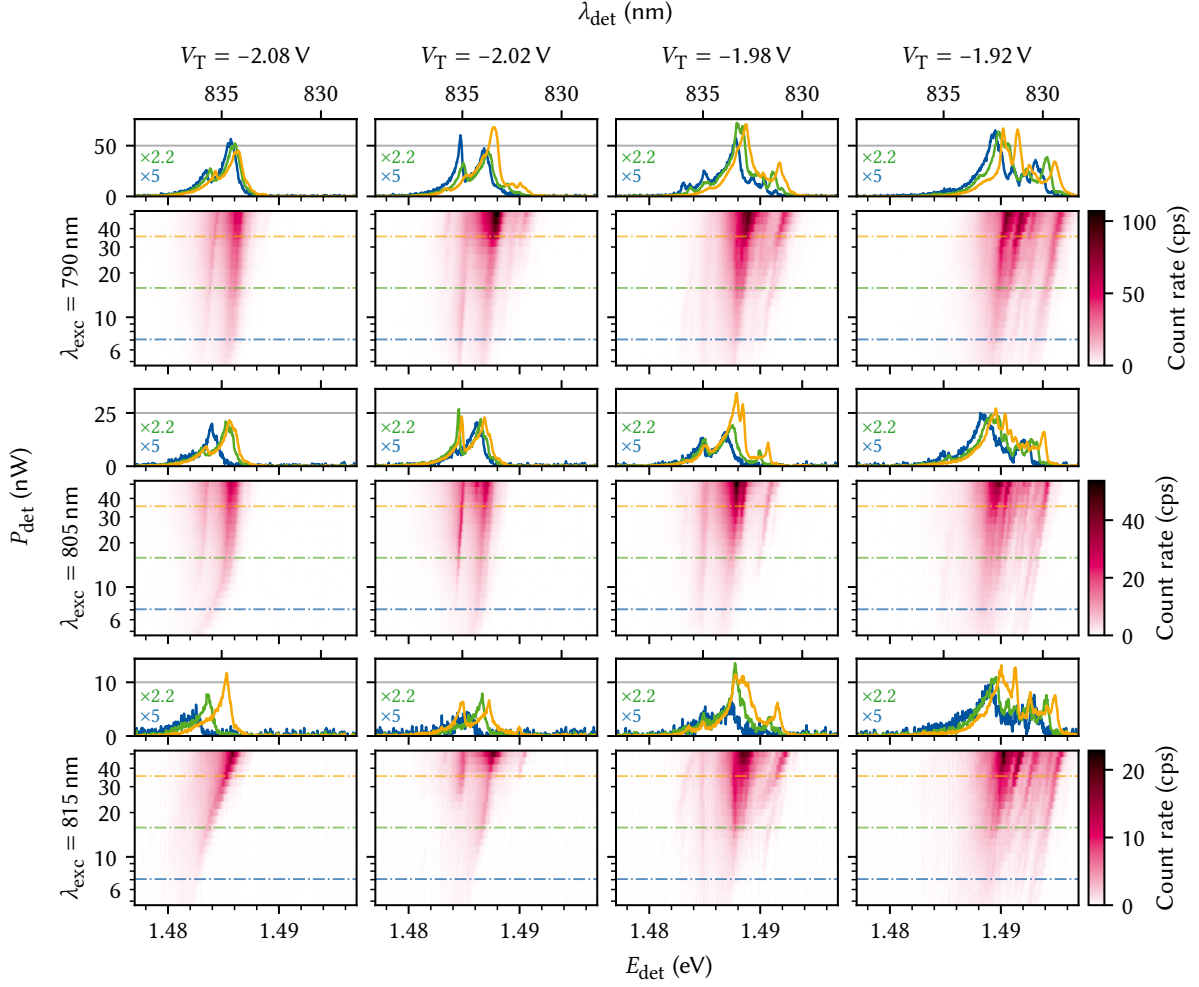


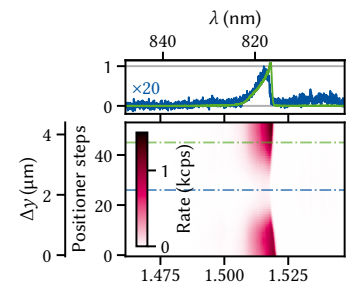
**Figure 9.5:** Wide-range PL parameter sweep on a large exciton trap plotted as function of excitation power and detection energy. Rows are data for three different excitation wavelengths, columns for four different top gate voltages  $V_T$  and share color and line cut scales. Line cuts are taken at the indicated positions of  $P_{\text{det}} = 7 \text{ nW}$ ,  $16 \text{ nW}$ , and  $35 \text{ nW}$  and drawn scaled by the fraction of excitation power with respect to  $35 \text{ nW}$ .

expect from fluctuations in the width of the QW by one atomic layer of GaAs with lattice constant  $a = 5.65 \text{ \AA}$  for the design well width  $L = 20 \text{ nm}$  (Section 7.1).

### 9.1.3 Spatial dependence

As mentioned several times already, the nanopositioners on which the sample is mounted show hysteresis and are therefore not suited for reproducible spatial maps of the sample. The hysteresis is due to the non-adiabaticity of the method of movement in the so-called slip-stick mode (*cf.* Chapter 2). What is more, the resistive position readout is also fairly unreliable below, say,  $5 \mu\text{m}$  resolution. Nonetheless, we can at the very least perform simple one-dimensional sweeps after manually positioning the sample at a given starting position. A more sophisticated algorithmic approach using feature detection may allow also two-dimensional maps with a reasonable accuracy.

Figure 9.6 shows the PL collected from the sample as the positioner is stepped perpendicularly across an unbiased gate. The vertical axis also



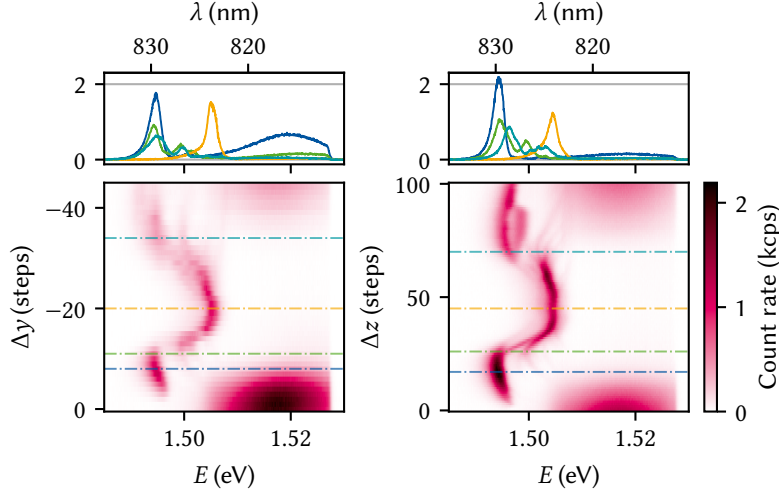


**Figure 9.7:** PL of a large exciton trap as function of position perpendicular (left) and parallel (right) to gravity. The trap is biased so that the emission is Stark-shifted towards lower energy. Upper panels show line cuts taken along the dash-dotted lines in the lower panels, demonstrating fairly identical behavior along both axes.

gives a position coordinate which is computed from the steps by fitting the position readout once hysteresis has worn off. The blue and green dash-dotted line correspond to the center of and beside the gate, respectively, with line cuts drawn in the upper panel. Clearly, the PL intensity is quenched significantly by the gate, beyond what one could expect from simple reflection and absorption of laser and PL radiation. I perform transfer-matrix method (TMM) simulations to explain this behavior in Section 9.3 (see also Figure 9.2). Curiously, the map also shows a shifting of the Fermi edge close to the gate. This behavior was consistently observed on this sample next to an unusual PL line shape (*cf.* Figure 9.1). The former effect could potentially be caused by band-deformation due to strain from the metallic gates.

Next, I show two sweeps along orthogonal axes across the biased exciton trap discussed before in Figures 9.3 to 9.5 and 9.8. While this is not unequivocal proof of zero-dimensional confinement, it does suggest that the effective exciton potential is lowered in a laterally localized fashion. The left panel of Figure 9.7 shows a scan along the in-plane axis perpendicular to gravity, while the right shows the in-plane axis parallel and against gravity. Regrettably, the resistive position readout did not yield anything but noise in these measurements, prohibiting a conversion of positioner steps into relative position as before. Both scans were acquired with the sample voltage applied to the positioners (30 V), which is the same used in Figure 9.6 as well. We can hence roughly expect 10 steps to correspond to 1  $\mu\text{m}$  in  $y$  direction. Naturally, a single step against gravity displaces the sample by a smaller amount compared to the perpendicular direction, but given the circular shape of the trap and the similarity of the PL features the displayed ranges should be roughly the same. The upper panels show line cuts taken at the positions indicated by dash-dotted lines in the lower panels as usual. Both sweeps display very similar features. In the center of the trap, the Stark-shifted emission line consists of a single peak. Towards the edges, two surprising effects take place: first, the Stark shift of the dominant peak increases in magnitude, and second, a large number of additional, faint lines appear. The increase in effective electric field towards the edge of an exciton trap is reminiscent of the simulation of the same type of experiment for an undoped QW by Descamps [8, Figure 6.4], although it was not explained there. Indeed, it also appears to be in conflict with Figure 2.16 *ibid.*, where a monotonic increase in effective exciton potential as function of distance

from the trap center closer to our intuition was predicted. In the device under study here, there is of course a 2DEG whose presence towards the edge of the trap screens the voltages, in theory contributing to an attenuation of the Stark shift. Why we observe to opposite is thus quite puzzling.

The second surprising feature seen in Figure 9.7 is the addition of faint lines that appear to branch out from the main exciton line as the laser spot is moved away from the center of the trap. These could be related to the lines observed in Figure 9.5.

## 9.2 Photoluminescence excitation spectroscopy

[54, 55] [41, 56]

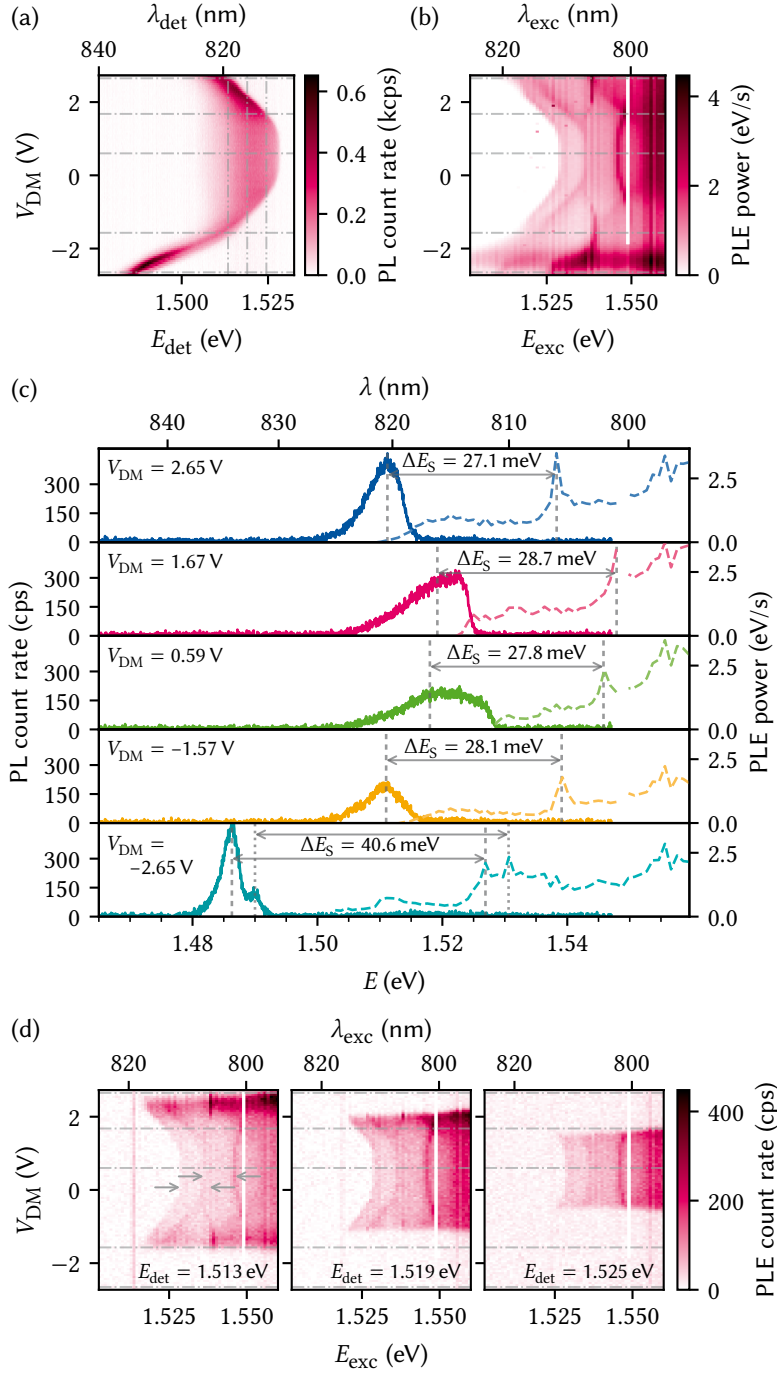


**Figure 9.8:** PL (solid lines) and photoluminescence excitation (PLE) (dashed lines) for different voltages  $V_{DM}$  (cf. Figure 9.3). The PLE data points correspond to PL spectra integrated up to the laser line. Arrows indicate the Stokes shift  $\Delta E_S$ , which is approximately constant (although assignment of the gap peak is difficult for 1.57 V and 0 V) until the 2DEG is fully depleted and the exciton resonance shifts quadratically with the electric field. The features at 1.55 eV do not shift with the voltage and are thus likely unrelated to the trap. For the largest voltage, there is another peak at 1.51 eV whose origin is unclear.

### 9.3 Transfer-matrix method simulations of the membrane structure

The TMM is a computationally efficient method of obtaining the electric field in layered structures. In this section, I perform simulations of the heterostructure membranes investigated in this part of the present thesis using the PyMoosh package [57] to elucidate the observed quenching of PL when illuminating gate electrodes as well as the overall optical efficiency.<sup>15</sup> I will first briefly recap the simulation method following Reference 57. For more details, refer to *ibid.* and references therein.

Consider a layered structure along  $z$  with interfaces at  $z_i, i \in \{0, 1, \dots, N+1\}$  that is translationally invariant along  $x$  and  $y$ . Each layer  $i$  may consist of a different dielectric material characterized by a (complex) relative permittivity  $\epsilon_{r,i}$ .<sup>16</sup> The electric field component along  $y$  of an electromagnetic wave transverse electric (TE) mode originating in some far away point satisfies the Helmholtz equation

$$\frac{\partial^2 E_y}{\partial z^2} + \gamma_i^2 E_y = 0, \quad (9.5)$$

where  $\gamma_i = \sqrt{\epsilon_{r,i} k_0^2 - k_x^2}$  with  $k_0 = \omega/c$  the wave vector in vacuum and  $k_x$  the component along  $x$ . In layer  $i$  of the structure, the solution to Equation 9.5 may be written as a superposition of plane waves incident and reflected on the lower and upper interfaces [57],

$$\begin{cases} E_{y,i}(z) = A_i^+ \exp\{i\gamma_i[z - z_i]\} + B_i^+ \exp\{-i\gamma_i[z - z_i]\}, \\ E_{y,i}(z) = A_i^- \exp\{i\gamma_i[z - z_{i+1}]\} + B_i^- \exp\{-i\gamma_i[z - z_{i+1}]\}, \end{cases} \quad (9.6)$$

where the coefficients with superscript  $+$  ( $-$ ) are referenced to the phase at the upper (lower) interface, respectively. Matching these solutions at  $z = z_i$  for all  $i$  to satisfy the interface conditions imposed by Maxwell's equations gives rise to a linear system of equations, the solution to which can be obtained through several different methods.

A particularly simple method is the transfer-matrix method ( $T$ -matrix formalism), which corresponds to writing the interface conditions at  $z = z_i$  as the matrix equation

$$\begin{pmatrix} A_{i+1}^+ \\ B_{i+1}^+ \end{pmatrix} = T_{i,i+1} \begin{pmatrix} A_i^- \\ B_i^- \end{pmatrix} \quad (9.7)$$

with

$$T_{i,i+1} = \frac{1}{2\gamma_{i+1}} \begin{pmatrix} \gamma_i + \gamma_{i+1} & \gamma_i - \gamma_{i+1} \\ \gamma_i - \gamma_{i+1} & \gamma_i + \gamma_{i+1} \end{pmatrix} \quad (9.8)$$

the transfer matrix for interface  $i$ . Connecting the coefficients for adjacent interfaces within a layer of height  $h_i = z_{i+1} - z_i$  requires propagating the phase,

$$\begin{pmatrix} A_i^- \\ B_i^- \end{pmatrix} = C_i \begin{pmatrix} A_i^+ \\ B_i^+ \end{pmatrix}, \quad (9.9)$$

with

$$C_i = \exp\{\text{diag}(-i\gamma_i h_i, i\gamma_i h_i)\}. \quad (9.10)$$

Iterating Equations 9.8 and 9.10, the total transfer matrix  $T = T_{0,N+1}$  then

15: Strictly speaking, the term TMM only refers to one of the several formalisms implemented in the PyMoosh package. While fast, it is not the most numerically stable, and other methods may be preferred if wall time is not a limiting issue.

16: We disregard magnetic materials with relative permeability  $\mu_r \neq 1$  for simplicity.

reduces to the matrix product

$$T = T_{N,N+1} \prod_{i=0}^{N-1} T_{i,i+1} C_i. \quad (9.11)$$

From  $T$ , the reflection and transmission coefficients can be obtained as  $r = A_0^- = -T_{01}/T_{00}$  and  $t = B_{N+1}^+ = rT_{10} + T_{11}$ . Taking the absolute value square of reflection and transmission coefficients then yields the reflectance  $\mathcal{R}$  and the transmittance  $\mathcal{T}$ , which correspond to the fraction of total incident power being reflected and transmitted, respectively. To obtain the absorptance  $\mathcal{A}$ , the fraction of power being absorbed, in layer  $i$ , one can compute the difference of the  $z$ -components of the Poynting vectors (cf. Equation 3.18) at the top of layers  $i$  and  $i + 1$ . In the TE case considered here, Equation 3.18 reduces to [57]

$$S_i = \text{Re} \left[ \frac{\gamma_i^*}{\gamma_0} (A_i^+ - B_i^+) (A_i^+ + B_i^+) \right] \quad (9.12)$$

and is hence straightforward to extract from the calculation of either the  $S$  or  $T$  matrices.

Equation 9.11 is simple to evaluate on a computer, making this method attractive for numerical applications. However, the opposite signs in the argument of the exponentials in Equation 9.10 can lead to instabilities for evanescent waves ( $\gamma_i \in \mathbb{C}$ ) due to finite-precision floating point arithmetic [58]. Rewriting Equation 9.8 to have incoming and outgoing fields on opposite sides of the equality alleviates this issue while sacrificing the simple matrix-multiplication composition rule in what is known as the scattering matrix ( $S$ -matrix) formalism. Finally, note that for a thorough accounting of in- and out-going field amplitudes, excitonic effects should be included, for example using the approach by D'Andrea and Del Sole [59].

Beyond the calculation of the aforementioned coefficients, the TMM formalism also allows to compute the full spatial dependence of the fields. Two cases are implemented in PyMoosh: irradiation of the layered structured with a Gaussian beam rather than plane waves of infinite extent, and a current line source inside the structure. In the first case, the previously assumed translational invariance along  $x$  leading to a plane-wave spatial dependence is replaced by a superposition of plane waves weighted with a normally distributed amplitude,<sup>17</sup>

$$E_{y,i}(x, z) = \exp(ik_x x) \rightarrow \int \frac{dk_x}{2\pi} \mathcal{E}_0(k_x) E_{y,i}(k_x, z) \exp(ik_x x), \quad (9.13)$$

with (cf. Equation 4.6)

$$\mathcal{E}_0(k_x) = \frac{w_0}{2\sqrt{\pi}} \exp \left\{ -ik_x x_0 - \left[ \frac{w_0 k_x}{2} \right]^2 \right\} \quad (9.14)$$

and

$$E_{y,i}(k_x, z) = A_i^- \exp\{i\gamma_i(k_x)[z - z_{i+1}]\} + B_i^+ \exp\{-i\gamma_i(k_x)[z - z_i]\}, \quad (9.15)$$

and where we considered only normal incidence for simplicity.

In the second case, Langevin et al. [57] consider an AC current  $I$  flowing through a translationally invariant, one-dimensional wire along  $y$  at  $x = x_s$ . This introduces a source term into the Helmholtz equation, Equa-

17: I.e., the inverse Fourier transform of  $\mathcal{E}_0(k_x) E_{y,i}(k_x, z)$ .

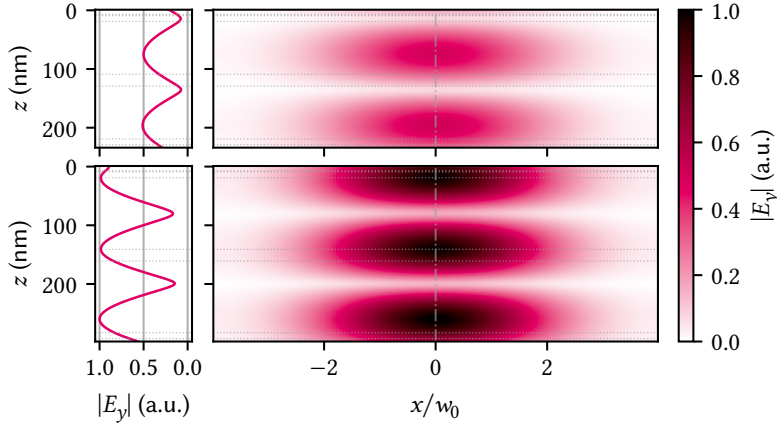


**Figure 9.9:** Absolute value of the electric field inside the double-gated heterostructure under illumination with a Gaussian beam at  $\lambda = 825$  nm from the top. Top (bottom) panels show the structure with the default (optimized) barrier thickness of 90 nm (122 nm), respectively. Dotted horizontal lines indicate interfaces between different materials while the vertical dash-dotted line indicates the position of the line cuts shown in the left column. Increasing the thickness of the barrier has two beneficial effects; first, the overall field intensity inside the structure is higher by a factor of two, and second, there is a peak rather than a knot in the QW at a depth of  $\sim 120$  nm ( $\sim 150$  nm), leading to enhanced absorption.

tion 9.5, which, upon Fourier transforming in  $x$  direction, leads to

$$\frac{\partial^2 \hat{E}_y}{\partial z^2} + \gamma_i^2 \hat{E}_y = -i\omega\mu_0 I \delta(z) \exp(ik_x x_s). \quad (9.16)$$

The electric field  $\hat{E}_{y,i}(k_x, z)$  is thus proportional to the Green's function of Equation 9.16 and can be obtained using a similar procedure as in the case of a distant source incident on the structure by matching the interface conditions. Performing the inverse Fourier transform by means of Equation 9.13 with constant weights,  $\mathcal{E}_0(k_x) \equiv 1$ , then yields the two-dimensional spatial distribution of the electric field,  $E_{y,i}(x, z)$ .

**Table 9.1:** Absorptance  $\mathcal{A}$  and reflectance  $\mathcal{R}$  in the QW for different configurations of the heterostructure. “Bare” is the standard structure without gate electrodes. “TG” and “BG” are with a gate on either the top or bottom side. “TG+BG” is with gates on both sides as on a trap site.

	$\mathcal{A}$ (%)	$\mathcal{R}$ (%)
Bare	2.9	22.4
TG	1.8	42.0
BG	0.5	82.7
TG+BG	0.4	84.8

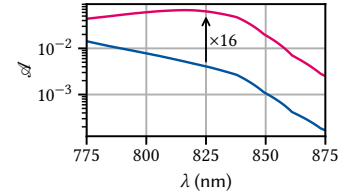


**Figure 9.10:** QW absorptance  $\mathcal{A}$  in a heterostructure with default (blue) and optimized (magenta) barrier thickness and top and bottom gates as function of wavelength. Optimization was performed at 825 nm using the differential evolution algorithm implemented in PyMoosh, resulting in a barrier thickness of 122 nm and an absorptance better by a factor of 16 at 6.3 %.

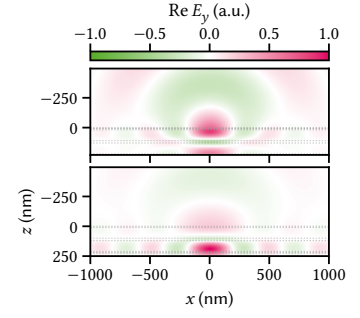


**Figure 9.11:** Real part of the electric field emitted by a current line located in the QW (black point) for different cases of the unoptimized structure. From top to bottom: bare heterostructure, top gate, bottom gate, top and bottom gate. The half space  $z < 0$  is the air above the membrane in the direction of the objective lens and the dotted lines indicate interfaces between materials. Evidently, the bottom gate reduces the amplitude in the upper half of the membrane and thereby the outcoupling efficiency compared to the structures with just a top gate, consistent with what is observed in the experiment.

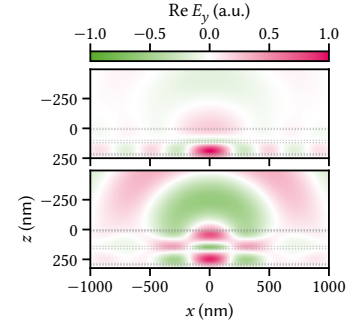


**Figure 9.12:** Real part of the electric field emitted by a current line located in the QW (black point) for the default (top) and optimized (bottom) structures with top and bottom gates. Optimizing the barrier thickness for absorption in the QW evidently also drastically improves the outcoupling efficiency into the half-space  $z < 0$ .





## **Part IV**

# **A FILTER-FUNCTION FORMALISM FOR UNITAL QUANTUM OPERATIONS**

# **APPENDIX**

# Additional TMM simulations



## C.1 Dependence on epoxy thickness

## C.2 Optimization of the barrier thickness

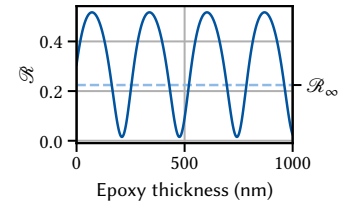


Figure C.1

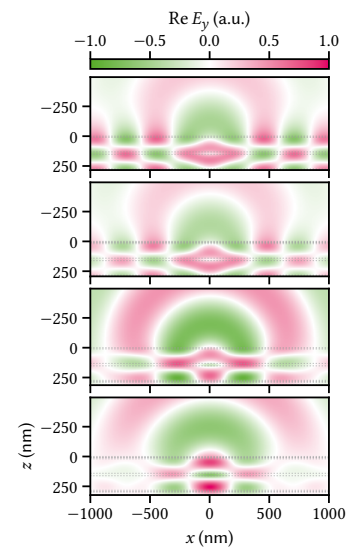
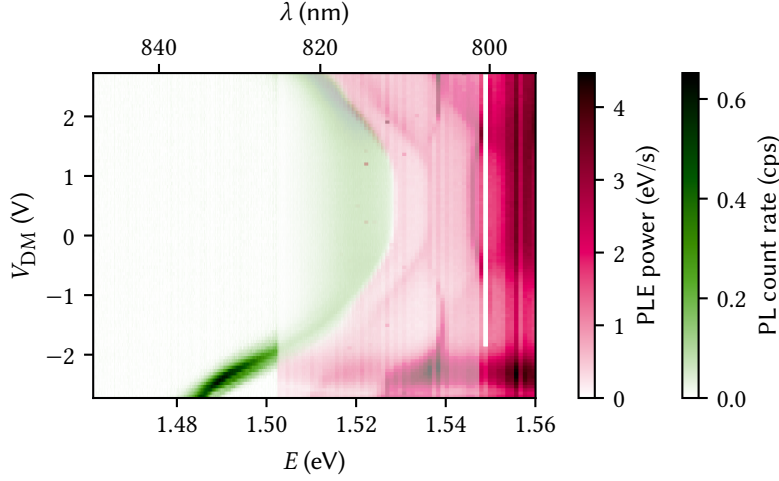


Figure C.2

# Additional measurements

D



**Table D.1:** Heterostructure parameters used in the present thesis. The doping density  $N_d$  is nominal, whereas the charge carrier density in the quantum well (QW),  $n$ , is computed using the nominal doping values with parameters given in Table D.2.

WAFER	$N_d$ (cm <sup>-3</sup> )	$n$ (cm <sup>-2</sup> )
M1_05_49	$6.5 \times 10^{17}$	$1.95 \times 10^{11}$
15460 (Honey)	$1.8 \times 10^{18}$	$4.26 \times 10^{11}$
15271 (Fig)	$8.0 \times 10^{17}$	$3.91 \times 10^{11}$

**Table D.2:** Simulation parameters used to compute the charge carrier density  $n$  in Table D.1.  $E_{DX}$  is the

PARAMETER	VALUE	UNIT
$E_{DX}^a$	-71.5	meV
$\Delta E_c^b$	240	meV
$m_c$	0.067	$m_e$
$\Delta z$	0.5	nm
$T$	10	mK
$V_{FP}^c$	0.76	V

- <sup>a</sup> Energy of the DX-center below the Fermi level.  
<sup>b</sup> Conduction band offset at the GaAs/Al-GaAs interface.  
<sup>c</sup> Fermi level pinning voltage.

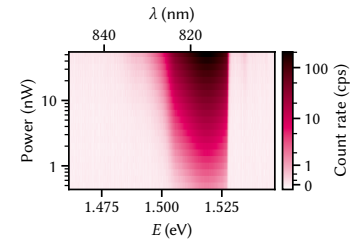


**Figure D.1**

# Bibliography

- [1] Thomas Ihn. *Semiconductor Nanostructures: Quantum States and Electronic Transport*. Oxford University Press, Nov. 26, 2009 (cited on pages 33, 42).
- [2] Horst L. Stormer. “Nobel Lecture: The Fractional Quantum Hall Effect.” In: *Reviews of Modern Physics* 71.4 (July 1, 1999), pp. 875–889. doi: [10.1103/RevModPhys.71.875](https://doi.org/10.1103/RevModPhys.71.875) (cited on page 33).
- [3] R. H. Harrell et al. “Fabrication of High-Quality One- and Two-Dimensional Electron Gases in Undoped GaAs/AlGaAs Heterostructures.” In: *Applied Physics Letters* 74.16 (Apr. 19, 1999), pp. 2328–2330. doi: [10.1063/1.123840](https://doi.org/10.1063/1.123840) (cited on page 33).
- [4] J. C. H. Chen et al. “Fabrication and Characterization of Ambipolar Devices on an Undoped AlGaAs/-GaAs Heterostructure.” In: *Applied Physics Letters* 100.5 (Jan. 30, 2012), p. 052101. doi: [10.1063/1.3673837](https://doi.org/10.1063/1.3673837) (cited on page 33).
- [5] Hai-Ou Li et al. “Fabrication and Characterization of an Undoped GaAs/AlGaAs Quantum Dot Device.” In: *Journal of Applied Physics* 116.17 (Nov. 3, 2014), p. 174504. doi: [10.1063/1.4900915](https://doi.org/10.1063/1.4900915) (cited on page 33).
- [6] L. A. Tracy, T. W. Hargett, and J. L. Reno. “Few-Hole Double Quantum Dot in an Undoped GaAs/AlGaAs Heterostructure.” In: *Applied Physics Letters* 104.12 (Mar. 24, 2014), p. 123101. doi: [10.1063/1.4868971](https://doi.org/10.1063/1.4868971) (cited on page 33).
- [7] Matthias E Rößler. “Contacting Backgated Two-dimensional Electron Gases for Quantum Dot Spin Qubits in GaAs.” MA thesis. Aachen: RWTH Aachen University, Sept. 2016 (cited on page 33).
- [8] Thomas Descamps. “Electrostatic Exciton Trap in a Thin Semiconductor Membrane for Optical Coupling to a GaAs Spin Qubit.” PhD thesis. Aachen: RWTH Aachen University, 2021 (cited on pages 33, 36–38, 41, 43–46, 48).
- [9] Sebastian Kindel. PhD thesis. Aachen: RWTH Aachen University, 2025 (cited on pages 33, 41).
- [10] Takafumi Fujita et al. “Distinguishing Persistent Effects in an Undoped GaAs/AlGaAs Quantum Well by Top-Gate-Dependent Illumination.” In: *Journal of Applied Physics* 129.23 (June 21, 2021), p. 234301. doi: [10.1063/5.0047558](https://doi.org/10.1063/5.0047558) (cited on page 33).
- [11] A. Shetty et al. “Effects of Biased and Unbiased Illuminations on Two-Dimensional Electron Gases in Dopant-Free GaAs/AlGaAs.” In: *Physical Review B* 105.7 (Feb. 7, 2022), p. 075302. doi: [10.1103/PhysRevB.105.075302](https://doi.org/10.1103/PhysRevB.105.075302) (cited on page 33).
- [12] Huiyi Wang. “Stability Investigation of GaAs Quantum Dot Devices under Illumination.” MA thesis. Aachen: RWTH Aachen University, Nov. 4, 2023. 65 pp. (cited on page 33).
- [13] Maxim Reznikov. “Investigating Device Stability and Exploring New Materials for Semiconductor Spin Qubit Optical Interfaces.” MA thesis. Aachen: RWTH Aachen University, June 2024 (cited on page 33).
- [14] D. Kamburov et al. “Use of Micro-Photoluminescence as a Contactless Measure of the 2D Electron Density in a GaAs Quantum Well.” In: *Applied Physics Letters* 110.26 (June 26, 2017), p. 262104. doi: [10.1063/1.4985439](https://doi.org/10.1063/1.4985439) (cited on pages 33, 42).
- [15] I. Vurgaftman, J. R. Meyer, and L. R. Ram-Mohan. “Band Parameters for III–V Compound Semiconductors and Their Alloys.” In: *Journal of Applied Physics* 89.11 (June 2001), pp. 5815–5875. doi: [10.1063/1.1368156](https://doi.org/10.1063/1.1368156) (cited on pages 33, 43).
- [16] D. A. B. Miller et al. “Band-Edge Electroabsorption in Quantum Well Structures: The Quantum-Confined Stark Effect.” In: *Physical Review Letters* 53.22 (Nov. 26, 1984), pp. 2173–2176. doi: [10.1103/PhysRevLett.53.2173](https://doi.org/10.1103/PhysRevLett.53.2173) (cited on pages 33, 35).
- [17] John H. Davies. *The Physics of Low-Dimensional Semiconductors: An Introduction*. Cambridge: Cambridge Univ. Press, 2009. 438 pp. (cited on pages 33, 35–38).
- [18] G. D. Mahan. “Excitons in Degenerate Semiconductors.” In: *Physical Review* 153.3 (Jan. 15, 1967), pp. 882–889. doi: [10.1103/PhysRev.153.882](https://doi.org/10.1103/PhysRev.153.882) (cited on page 34).
- [19] G. D. Mahan. “Excitons in Metals.” In: *Physical Review Letters* 18.12 (Mar. 20, 1967), pp. 448–450. doi: [10.1103/PhysRevLett.18.448](https://doi.org/10.1103/PhysRevLett.18.448) (cited on page 34).

- [20] M. S. Skolnick et al. "Observation of a Many-Body Edge Singularity in Quantum-Well Luminescence Spectra." In: *Physical Review Letters* 58.20 (May 18, 1987), pp. 2130–2133. doi: [10.1103/PhysRevLett.58.2130](https://doi.org/10.1103/PhysRevLett.58.2130) (cited on pages 34, 42).
- [21] T. Mélin and F. Laruelle. "Fermi-Edge Singularities in  $\text{Al}_x\text{Ga}_{1-x}\text{As}$  Quantum Wells: Extrinsic versus Many-Body Scattering Processes." In: *Physical Review Letters* 85.4 (July 24, 2000), pp. 852–855. doi: [10.1103/PhysRevLett.85.852](https://doi.org/10.1103/PhysRevLett.85.852) (cited on page 34).
- [22] A. Gabbay et al. "Effect of Valence Subband Dispersion on Near-Band-Gap Transitions in  $\text{GaAs} / \text{Al}_x\text{Ga}_{1-x}\text{As}$  Quantum Wells Containing a Two-Dimensional Electron Gas." In: *Physical Review B* 77.16 (Apr. 21, 2008), p. 165329. doi: [10.1103/PhysRevB.77.165329](https://doi.org/10.1103/PhysRevB.77.165329) (cited on pages 34, 42).
- [23] Lucio Claudio Andreani and Alfredo Pasquarello. "Accurate Theory of Excitons in  $\text{GaAs-Ga}_{1-x}\text{Al}_x\text{As}$  Quantum Wells." In: *Physical Review B* 42.14 (Nov. 15, 1990), pp. 8928–8938. doi: [10.1103/PhysRevB.42.8928](https://doi.org/10.1103/PhysRevB.42.8928) (cited on page 34).
- [24] G. D. Gilliland. "Photoluminescence Spectroscopy of Crystalline Semiconductors." In: *Materials Science and Engineering: R: Reports* 18.3 (1997), pp. 99–399. doi: [10.1016/S0927-796X\(97\)80003-4](https://doi.org/10.1016/S0927-796X(97)80003-4) (cited on page 34).
- [25] Tania Palmieri et al. "Mahan Excitons in Room-Temperature Methylammonium Lead Bromide Perovskites." In: *Nature Communications* 11.1 (Feb. 12, 2020), p. 850. doi: [10.1038/s41467-020-14683-5](https://doi.org/10.1038/s41467-020-14683-5) (cited on page 34).
- [26] N. F. Mott. "Metal-Insulator Transition." In: *Reviews of Modern Physics* 40.4 (Oct. 1, 1968), pp. 677–683. doi: [10.1103/RevModPhys.40.677](https://doi.org/10.1103/RevModPhys.40.677) (cited on page 34).
- [27] André Schleife et al. "Optical Absorption in Degenerately Doped Semiconductors: Mott Transition or Mahan Excitons?" In: *Physical Review Letters* 107.23 (Nov. 30, 2011), p. 236405. doi: [10.1103/PhysRevLett.107.236405](https://doi.org/10.1103/PhysRevLett.107.236405) (cited on page 34).
- [28] Thomas Olsen et al. "Simple Screened Hydrogen Model of Excitons in Two-Dimensional Materials." In: *Physical Review Letters* 116.5 (Feb. 2, 2016), p. 056401. doi: [10.1103/PhysRevLett.116.056401](https://doi.org/10.1103/PhysRevLett.116.056401) (cited on page 34).
- [29] R. C. Miller, D. A. Kleinman, and A. C. Gossard. "Energy-Gap Discontinuities and Effective Masses for  $\text{GaAs} - \text{Al}_x\text{Ga}_{1-x}\text{As}$  Quantum Wells." In: *Physical Review B* 29.12 (June 15, 1984), pp. 7085–7087. doi: [10.1103/PhysRevB.29.7085](https://doi.org/10.1103/PhysRevB.29.7085) (cited on pages 35, 36, 38).
- [30] A. Rabinovitch and J. Zak. "Electrons in Crystals in a Finite-Range Electric Field." In: *Physical Review B* 4.8 (Oct. 15, 1971), pp. 2358–2370. doi: [10.1103/PhysRevB.4.2358](https://doi.org/10.1103/PhysRevB.4.2358) (cited on page 35).
- [31] D. A. B. Miller et al. "Electric Field Dependence of Optical Absorption near the Band Gap of Quantum-Well Structures." In: *Physical Review B* 32.2 (July 15, 1985), pp. 1043–1060. doi: [10.1103/PhysRevB.32.1043](https://doi.org/10.1103/PhysRevB.32.1043) (cited on pages 35, 36).
- [32] A. V. Kavokin. "Exciton Oscillator Strength in Quantum Wells: From Localized to Free Resonant States." In: *Physical Review B* 50.11 (Sept. 15, 1994), pp. 8000–8003. doi: [10.1103/PhysRevB.50.8000](https://doi.org/10.1103/PhysRevB.50.8000) (cited on pages 36, 37).
- [33] E. Karimi et al. "Radial Quantum Number of Laguerre-Gauss Modes." In: *Physical Review A* 89.6 (June 16, 2014), p. 063813. doi: [10.1103/PhysRevA.89.063813](https://doi.org/10.1103/PhysRevA.89.063813) (cited on page 36).
- [34] Robert C. Hilborn. "Einstein Coefficients, Cross Sections,  $f$  Values, Dipole Moments, and All That." In: *American Journal of Physics* 50.11 (Nov. 1, 1982), pp. 982–986. doi: [10.1119/1.12937](https://doi.org/10.1119/1.12937) (cited on page 37).
- [35] A. Larsson et al. "Tunable Superlattice P-i-n Photodetectors: Characteristics, Theory, and Application." In: *IEEE Journal of Quantum Electronics* 24.5 (May 1988), pp. 787–801. doi: [10.1109/3.195](https://doi.org/10.1109/3.195) (cited on pages 38, 45).
- [36] R. C. Miller and D. A. Kleinman. "Excitons in  $\text{GaAs}$  Quantum Wells." In: *Journal of Luminescence* 30.1 (Feb. 1, 1985), pp. 520–540. doi: [10.1016/0022-2313\(85\)90075-4](https://doi.org/10.1016/0022-2313(85)90075-4) (cited on page 39).
- [37] Satoshi Kako et al. "Biexciton in Single  $\text{GaN/AlN}$  Self-Assembled Quantum Dots." In: *Conference on Lasers and Electro-Optics/International Quantum Electronics Conference and Photonic Applications Systems Technologies*. International Quantum Electronics Conference. San Francisco, California: OSA, 2004, IThC5. doi: [10.1364/IQEC.2004.IThC5](https://doi.org/10.1364/IQEC.2004.IThC5) (cited on page 39).

- [38] G.E. Dialynas et al. “Anti-Binding of Biexcitons in (211)B InAs/GaAs Piezoelectric Quantum Dots.” In: *Physica E: Low-dimensional Systems and Nanostructures* 40.6 (Apr. 2008), pp. 2113–2115. DOI: [10.1016/j.physe.2007.10.036](#) (cited on page 39).
- [39] S. Amloy et al. “Size Dependent Biexciton Binding Energies in GaN Quantum Dots.” In: *Applied Physics Letters* 99.25 (Dec. 19, 2011), p. 251903. DOI: [10.1063/1.3670040](#) (cited on page 39).
- [40] Gleb Finkelstein, Hadas Shtrikman, and Israel Bar-Joseph. “Optical Spectroscopy of a Two-Dimensional Electron Gas near the Metal-Insulator Transition.” In: *Physical Review Letters* 74.6 (Feb. 6, 1995), pp. 976–979. DOI: [10.1103/PhysRevLett.74.976](#) (cited on page 39).
- [41] Axel Esser et al. “Photoluminescence and Radiative Lifetime of Trions in GaAs Quantum Wells.” In: *Physical Review B* 62.12 (Sept. 15, 2000), pp. 8232–8239. DOI: [10.1103/PhysRevB.62.8232](#) (cited on pages 39, 49).
- [42] Israel Bar-Joseph. “Trions in GaAs Quantum Wells.” In: *Semiconductor Science and Technology* 20.6 (June 1, 2005), R29–R39. DOI: [10.1088/0268-1242/20/6/R01](#) (cited on page 39).
- [43] Elias Burstein. “Anomalous Optical Absorption Limit in InSb.” In: *Physical Review* 93.3 (Feb. 1, 1954), pp. 632–633. DOI: [10.1103/PhysRev.93.632](#) (cited on page 42).
- [44] T. S. Moss. “The Interpretation of the Properties of Indium Antimonide.” In: *Proceedings of the Physical Society. Section B* 67.10 (Oct. 1954), p. 775. DOI: [10.1088/0370-1301/67/10/306](#) (cited on page 42).
- [45] A. Pinczuk et al. “Optical Processes of 2D Electron Plasma in GaAs-(AlGa)As Heterostructures.” In: *Solid State Communications* 50.8 (May 1, 1984), pp. 735–739. DOI: [10.1016/0038-1098\(84\)90975-X](#) (cited on pages 42, 43).
- [46] R. Ulbrich. “Energy Relaxation of Photoexcited Hot Electrons in GaAs.” In: *Physical Review B* 8.12 (Dec. 15, 1973), pp. 5719–5727. DOI: [10.1103/PhysRevB.8.5719](#) (cited on page 42).
- [47] Hendrik Bluhm, *poisson\_schroedinger\_1D* May 14, 2024 (cited on page 43).
- [48] S. C. Jain et al. “Modified Simple Expression for Bandgap Narrowing in N-Type GaAs.” In: *Solid-State Electronics* 35.5 (May 1, 1992), pp. 639–642. DOI: [10.1016/0038-1101\(92\)90030-G](#) (cited on page 43).
- [49] Thomas Descamps et al. “Semiconductor Membranes for Electrostatic Exciton Trapping in Optically Addressable Quantum Transport Devices.” In: *Phys. Rev. Appl.* 19.4 (Apr. 28, 2023), p. 044095. DOI: [10.1103/PhysRevApplied.19.044095](#) (cited on page 44).
- [50] G.N. Nguyen et al. “Influence of Molecular Beam Effusion Cell Quality on Optical and Electrical Properties of Quantum Dots and Quantum Wells.” In: *Journal of Crystal Growth* 550 (Nov. 2020), p. 125884. DOI: [10.1016/j.jcrysgro.2020.125884](#) (cited on page 44).
- [51] H. Schneider and K. V. Klitzing. “Thermionic Emission and Gaussian Transport of Holes in a GaAs/ Al<sub>x</sub>Ga<sub>1-x</sub>As Multiple-Quantum-Well Structure.” In: *Physical Review B* 38.9 (Sept. 15, 1988), pp. 6160–6165. DOI: [10.1103/PhysRevB.38.6160](#) (cited on page 45).
- [52] A.M. Fox et al. “Quantum Well Carrier Sweep out: Relation to Electroabsorption and Exciton Saturation.” In: *IEEE Journal of Quantum Electronics* 27.10 (Oct. 1991), pp. 2281–2295. DOI: [10.1109/3.97272](#) (cited on page 45).
- [53] *Voigt Profile*. In: *Wikipedia*. June 12, 2025 (cited on page 46).
- [54] V. Huard et al. “Bound States in Optical Absorption of Semiconductor Quantum Wells Containing a Two-Dimensional Electron Gas.” In: *Physical Review Letters* 84.1 (Jan. 3, 2000), pp. 187–190. DOI: [10.1103/PhysRevLett.84.187](#) (cited on page 49).
- [55] G. Yusa, H. Shtrikman, and I. Bar-Joseph. “Onset of Exciton Absorption in Modulation-Doped GaAs Quantum Wells.” In: *Physical Review B* 62.23 (Dec. 15, 2000), pp. 15390–15393. DOI: [10.1103/PhysRevB.62.15390](#) (cited on page 49).
- [56] A. Esser, R. Zimmermann, and E. Runge. “Theory of Trion Spectra in Semiconductor Nanostructures.” In: *physica status solidi (b)* 227.2 (Oct. 2001), pp. 317–330. DOI: [10.1002/1521-3951\(200110\)227:2<317::AID-PSSB317>3.0.CO;2-S](#) (cited on page 49).
- [57] Denis Langevin et al. “PyMoosh: A Comprehensive Numerical Toolkit for Computing the Optical Properties of Multilayered Structures.” In: *Journal of the Optical Society of America B* 41.2 (Feb. 1, 2024), A67. DOI: [10.1364/JOSAB.506175](#) (cited on pages 51, 52).



- [58] Denny Dütz et al. “Distributed Bragg Reflectors for Thermal Isolation of Semiconductor Spin Qubits.” In preparation (cited on page 52).
- [59] A. D’Andrea and R. Del Sole. “Exciton Quantization and Polariton Propagation in Semiconductor Slabs: From Semi-Infinite Crystals to Quantum Wells.” In: *Physical Review B* 41.3 (Jan. 15, 1990), pp. 1413–1423. doi: [10.1103/PhysRevB.41.1413](https://doi.org/10.1103/PhysRevB.41.1413) (cited on page 52).
- [60] Maarten Baeten and Michiel Wouters. “Many-Body Effects of a Two-Dimensional Electron Gas on Trion-Polaritons.” In: *Physical Review B* 91.11 (Mar. 23, 2015), p. 115313. doi: [10.1103/PhysRevB.91.115313](https://doi.org/10.1103/PhysRevB.91.115313) (cited on page 55).
- [61] M. M. Glazov. “Optical Properties of Charged Excitons in Two-Dimensional Semiconductors.” In: *The Journal of Chemical Physics* 153.3 (July 21, 2020), p. 034703. doi: [10.1063/5.0012475](https://doi.org/10.1063/5.0012475) (cited on page 55).
- [62] Di Huang et al. “Quantum Dynamics of Attractive and Repulsive Polarons in a Doped MoSe<sub>2</sub> Monolayer.” In: *Physical Review X* 13.1 (Mar. 2, 2023), p. 011029. doi: [10.1103/PhysRevX.13.011029](https://doi.org/10.1103/PhysRevX.13.011029) (cited on page 55).

# Special Terms

## Numbers

**2DEG** two-dimensional electron gas. 33, 34, 39, 42–45, 49, 50

**2DHG** two-dimensional hole gas. 39

## C

**CCD** charge-coupled device. 40, 41

**CMOS** complementary metal-oxide-semiconductor. 41

**cw** continuous-wave. 41

## D

**DR** dilution refrigerator. 41

## E

**EBL** electron-beam lithography. 41, 43

## F

**FES** Fermi-edge singularity. 34, 42

## G

**GDQD** gate-defined quantum dot. 33

## M

**MMF** multi-mode fiber. 42

## N

**NA** numerical aperture. 42

## O

**OAQD** optically active quantum dot. 33

## P

**PL** photoluminescence. 34, 39, 41–48, 50, 51

**PLE** photoluminescence excitation. 50

**PSD** power spectral density. iii

## Q

**QCSE** quantum-confined Stark effect. 35, 36, 38

**QW** quantum well. 33–36, 38–44, 47, 48, 53, 54

## R

**RMS** root mean square. 41

## S

**SAQD** self-assembled quantum dot. 45

**SMF** single-mode fiber. 41, 42

## T

**TE** transverse electric. 51, 52

**TMM** transfer-matrix method. iv, 39, 48, 51, 52

# Declaration of Authorship

I, Tobias Hangleiter, declare that this thesis and the work presented in it are my own and has been generated by me as the result of my own original research.

I do solemnly swear that:

1. This work was done wholly or mainly while in candidature for the doctoral degree at this faculty and university;
2. Where any part of this thesis has previously been submitted for a degree or any other qualification at this university or any other institution, this has been clearly stated;
3. Where I have consulted the published work of others or myself, this is always clearly attributed;
4. Where I have quoted from the work of others or myself, the source is always given. This thesis is entirely my own work, with the exception of such quotations;
5. I have acknowledged all major sources of assistance;
6. Where the thesis is based on work done by myself jointly with others, I have made clear exactly what was done by others and what I have contributed myself;
7. Parts of this work have been published before as:

- [1] Pascal Cerfontaine, Tobias Hangleiter, and Hendrik Bluhm. “Filter Functions for Quantum Processes under Correlated Noise.” In: *Phys. Rev. Lett.* 127.17 (Oct. 18, 2021), p. 170403. DOI: [10.1103/PhysRevLett.127.170403](https://doi.org/10.1103/PhysRevLett.127.170403).
- [2] Thomas Descamps, Feng Liu, Tobias Hangleiter, Sebastian Kindel, Beata E. Kardynał, and Hendrik Bluhm. “Millikelvin Confocal Microscope with Free-Space Access and High-Frequency Electrical Control.” In: *Rev. Sci. Instrum.* 95.8 (Aug. 9, 2024), p. 083706. DOI: [10.1063/5.0200889](https://doi.org/10.1063/5.0200889).
- [3] Tobias Hangleiter, Pascal Cerfontaine, and Hendrik Bluhm. “Filter-Function Formalism and Software Package to Compute Quantum Processes of Gate Sequences for Classical Non-Markovian Noise.” In: *Phys. Rev. Research* 3.4 (Oct. 18, 2021), p. 043047. DOI: [10.1103/PhysRevResearch.3.043047](https://doi.org/10.1103/PhysRevResearch.3.043047).
- [4] Tobias Hangleiter, Pascal Cerfontaine, and Hendrik Bluhm. “Erratum: Filter-function Formalism and Software Package to Compute Quantum Processes of Gate Sequences for Classical Non-Markovian Noise [Phys. Rev. Research 3, 043047 (2021)].” In: *Phys. Rev. Res.* 6.4 (Oct. 16, 2024), p. 049001. DOI: [10.1103/PhysRevResearch.6.049001](https://doi.org/10.1103/PhysRevResearch.6.049001).

---

Aachen, August 5, 2025.